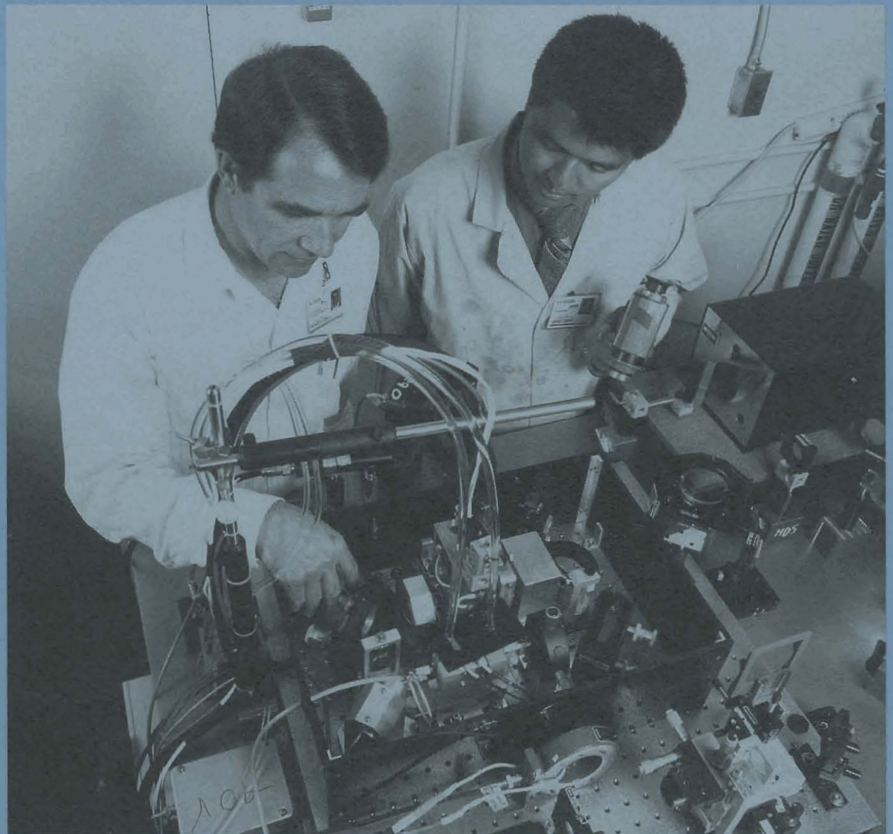


LLE Review

Quarterly Report



April-June 1992

Laboratory for Laser Energetics
College of Engineering and Applied Science
University of Rochester
250 East River Road
Rochester, New York 14623-1299



LLE Review

Quarterly Report

Editor: R. W. Short
(716) 275-4075

April–June 1992

Laboratory for Laser Energetics
College of Engineering and Applied Science
University of Rochester
250 East River Road
Rochester, New York 14623-1299



This report was prepared as an account of work conducted by the Laboratory for Laser Energetics and sponsored by New York State Energy Research and Development Authority, the University of Rochester, the U.S. Department of Energy, and other agencies.

Neither the above-named sponsors, nor any of their employees, makes any warranty, expressed or implied, or assumes any legal liability or responsibility for the accuracy, completeness, or usefulness of any information, apparatus, product, or process disclosed, or represents that its use would not infringe privately owned rights.

Reference herein to any specific commercial product, process, or service by trade name, mark manufacturer, or otherwise, does not necessarily constitute or imply its endorsement, recommendation, or favoring by the United States Government or any agency thereof or any other sponsor.

Results reported in the LLE Review should not be taken as necessarily final results as they represent active research. The views and opinions of authors expressed herein do not necessarily state or reflect those of any of the above sponsoring entities.

IN BRIEF

This volume of the LLE Review, covering the period April–June 1992, contains articles on laser-plasma interaction experiments in long-scale-length plasmas and on the theory of a new form of the stimulated Brillouin scattering instability. The advanced technology section includes reports on the optical response of superconducting films, the development of high-reflectance transport mirrors for the OMEGA Upgrade, and a new high-brightness mono-mode laser oscillator. Finally, the activities of the National Laser Users Facility and the GDL and OMEGA laser systems are summarized.

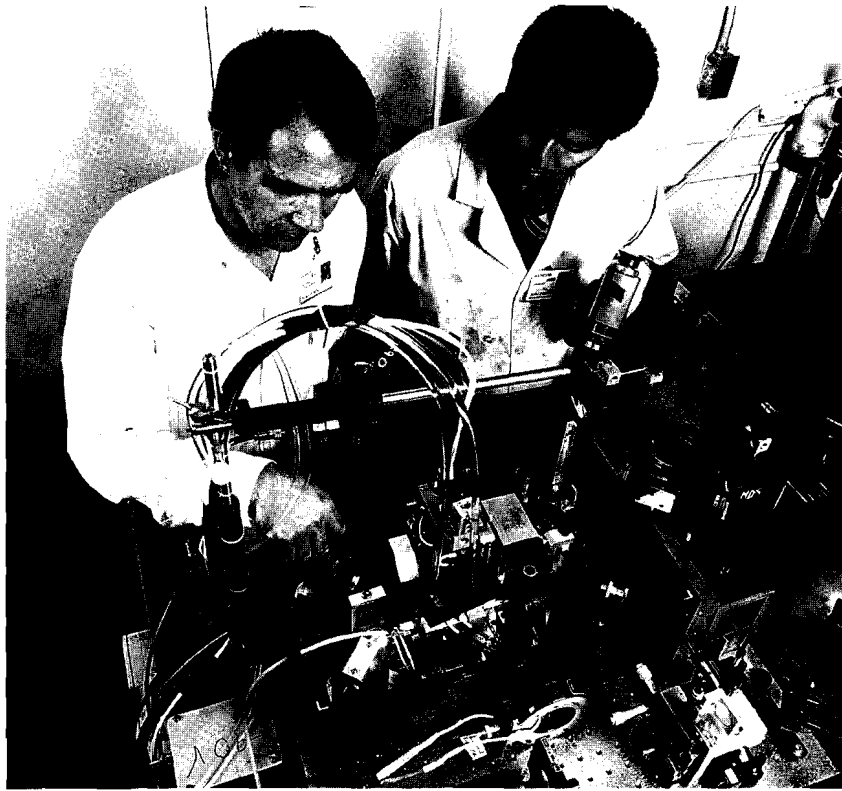
Highlights of the research reported in this issue are

- Experiments on long-scale-length plasmas, which model the conditions expected in the corona of a reactor-size target, have shown that smoothing by spectral dispersion (SSD), a technique developed at LLE to improve target irradiation uniformity, is also effective in reducing the level of stimulated Raman scattering. Scattered light produced by other instabilities was also observed and analyzed, providing information on the laser-plasma interaction.
- The theory of a new form of stimulated Brillouin scattering has been developed, in which inverse bremsstrahlung heating rather than ponderomotive force provides the driving nonlinearity. This form of the instability dominates in high-Z, low-temperature plasmas.

- The anomalous optical response of high-temperature superconductors to a laser beam has been measured. This effect may have an application as a fast (subnanosecond), high-power switch.
- It has been found that the intensity damage threshold for multilayer dielectric mirrors decreases with increasing angle of incidence. Methods of mitigating this effect for the OMEGA Upgrade transport mirrors (such as substitution of scandia for hafnia dielectrics) are proposed and discussed.
- An externally triggered, single-mode, Nd:YLF oscillator has been developed; possible applications include the generation of shaped synchronized pulses for OMEGA.

CONTENTS

	<i>Page</i>
IN BRIEF	iii
CONTENTS	v
Section 1 PROGRESS IN LASER FUSION	109
1.A Nonlinear Interactions in Long-Scale-Length Plasmas	109
1.B Thermal Stimulated Brillouin Scattering	125
Section 2 ADVANCED TECHNOLOGY DEVELOPMENTS	132
2.A Anomalous Optical Response of Superconducting Films	132
2.B High-Reflectance Transport-Mirror Development for the OMEGA Upgrade	139
2.C An Externally Triggered, Single-Mode, Nd:YLF Laser Oscillator	155
Section 3 NATIONAL LASER USERS FACILITY NEWS	165
Section 4 LASER SYSTEM REPORT	167
4.A GDL Facility Report	167
4.B OMEGA Facility Report	167
PUBLICATIONS AND CONFERENCE PRESENTATIONS	



Wolf Seka, Senior Scientist at the Laboratory for Laser Energetics, shows the operation of a recently developed, single-mode, Nd:YLF laser to graduate student Jong Chow.

Section 1

PROGRESS IN LASER FUSION

1.A Nonlinear Interactions in Long-Scale-Length Plasmas

Nonlinear laser-matter interaction processes relevant to inertial confinement fusion (ICF) have been studied experimentally and theoretically for over 25 years. During the last ten years emphasis has shifted to short-wavelength drivers ($\lambda_0 < 0.5 \mu\text{m}$) in order to maximize collisional coupling of the laser to the corona and minimize parametric laser-plasma interaction processes both near the critical density (n_c) surface (where the laser frequency ω_0 equals the plasma frequency ω_{pe}) and at lower densities. However, as experiments approach reactor dimensions, longer gradient scale lengths will increase the likelihood of significant excitation of these processes. To the extent that these processes involve the generation of plasma waves, they are potential sources of energetic electrons that could prevent efficient compression of the fuel. It is therefore important to continue to investigate these processes and their scaling laws under conditions approaching those of future larger-scale experiments. In particular, it is important to investigate the impact that beam-smoothing schemes have on these nonlinear processes.

In this article we will discuss a series of experiments on nonlinear interaction processes carried out on long-scale-length laser plasmas produced with the 24-beam OMEGA laser system. We will also offer our present understanding and interpretation of these experiments, although some of the suggestions are still rather tentative. The main processes considered are the two-plasmon decay (TPD) instability as evidenced by its traditional signature, the 3/2-harmonic emission from the plasma, and Raman scattering at densities below quarter critical.

Experimental Conditions

The background plasma for these experiments is furnished by first exploding mass-limited CH targets (0.6-mm diam, 6- μm thick) with eight primary beams.¹ This is followed by irradiation with eight secondary beams, delayed 0.6 ns relative to the primaries, which maintain the electron temperature $T_e > 1$ keV over a period of ~ 0.5 ns. Each laser beam has an energy of ~ 50 J at a vacuum wavelength of $\lambda_0 = 351$ nm, and the pulse duration is 0.6 ns. Furthermore, all beams are outfitted with distributed phase plates^{2,3} (DPP's) of 1.25-mm-diam hexagonal cell size yielding a minimum spot diameter of 380 μm (the first zero of the Airy pattern). These beams are strongly defocused (FWHM ≈ 450 μm) in order to irradiate the target as uniformly as possible at intensities $\leq 5 \times 10^{13}$ W/cm². Occasionally four to six tertiary beams have also been employed; these beams are delayed by 1 ns relative to the primaries, and their wavelength is 1.054 μm for increased absorption at late times. The production and characterization of the background plasma has been described extensively in Ref. 1.

This plasma is then irradiated by an interaction beam, also at $\lambda_0 = 351$ nm, with energy up to 60 J and a pulse duration also of 0.6 ns. The diameter of the DPP cells is increased by a factor of 2 for the interaction beam in order to obtain a maximum average interaction-beam intensity on target of $\sim 10^{15}$ W/cm². (This is the peak intensity in space and time of the envelope of the target-plane profile.) Some of the experiments were carried out with the addition of FM bandwidth ($f_{\text{FM}} = 10$ GHz, $\Delta\lambda/\lambda \leq 3 \times 10^{-4}$) and appropriate angular dispersion on all beams, resulting in beam smoothing by spectral dispersion⁴ (SSD). The primary diagnostics for these experiments were visible and UV spectroscopy, with and without time resolution. The directions of observations were chosen to optimize either the 3/2-harmonic emission (in the plane of polarization and at 20° from the backscatter direction) or the Raman signal (out-of-plane at 45° to the backscatter direction or direct backscatter).

Three-Halves Harmonic Spectra

The spectrum of this emission is always characterized by two peaks, usually asymmetrically displaced relative to $3\omega_0/2$, with the red-shifted component usually the stronger one. This signature is commonly attributed to Thomson (or Raman) scattering of interaction-beam photons off plasmons produced by the same beam through the TPD instability.^{5,6} We will call this process "self-scattering." In fact, the first observations of this instability were through its characteristic 3/2-harmonic emission.⁷ Various theories⁸ have since been proposed to precisely relate the TPD plasmons to the observed spectral features. However, none of these theories have been very successful⁹ and a generally accepted explanation of these features is still forthcoming.

The current experiments differ from previous ones in that we are able to change experimental conditions to highlight different features of the 3/2-harmonic spectra. Time resolution of these spectra has been found to be indispensable. Typical spectra for four different experimental conditions are shown in Fig. 51.1. Most features in Figs. 51.1(b)–51.1(e) are caused by the self-scattering, either from the primary beams [the weak signals on the left of

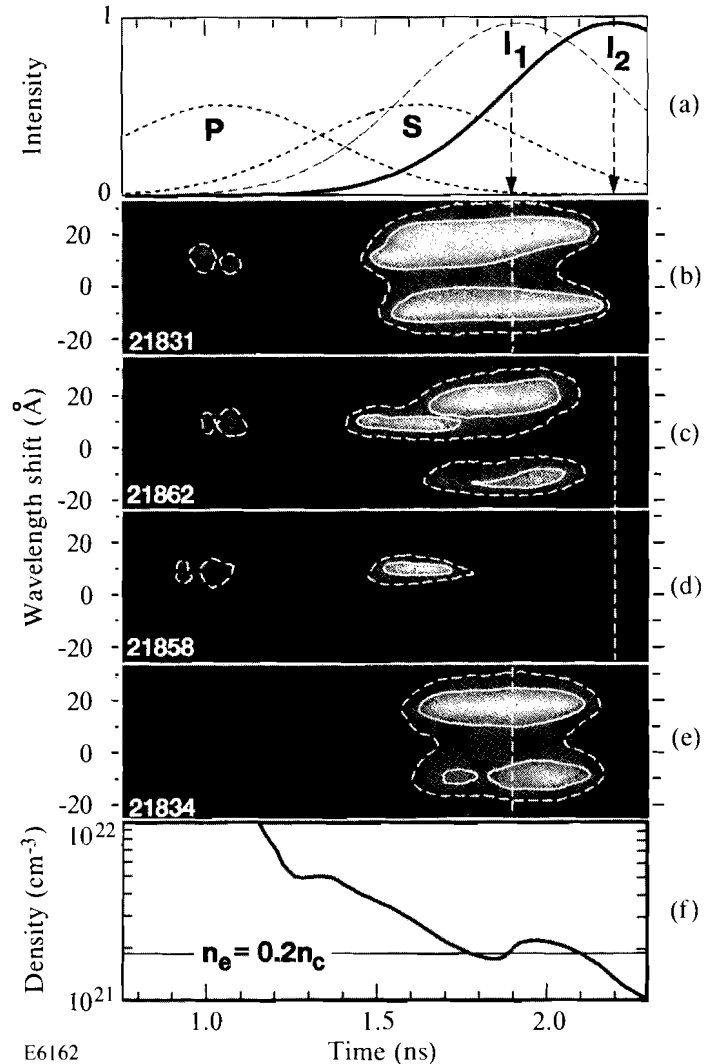


Fig. 51.1

Typical sequencing of the primary, secondary, and interaction beams (a), and time-resolved 3/2-harmonic spectra for different timings of the interaction beam: (b) 1.9 ns (I_1), (c) 2.2 ns (I_2), (d) 2.2 ns (I_2), and (e) 1.9 ns (I_1). Shots (b) through (d) had no FM bandwidth, while (e) had an SSD bandwidth of $\Delta\lambda/\lambda \approx 3 \times 10^{-4}$. In (f) the time evolution of the peak on-axis density calculated by SAGE (for primary and secondary beams only) is shown with the TPD Landau cutoff indicated at $n_e = 0.2 n_c$. The interaction-beam intensity is $\sim 10^{15}$ W/cm² for all figures but (d), for which it is $\sim 2 \times 10^{14}$ W/cm². The primary and secondary beam intensities are $\sim 5 \times 10^{13}$ W/cm². The wavelength of all beams is 351 nm. In (c) an additional six tertiary beams of $\lambda = 1054$ nm were added, with their peaks at 2 ns. The contour lines shown correspond roughly to the 50% and 20% of maximum intensity.

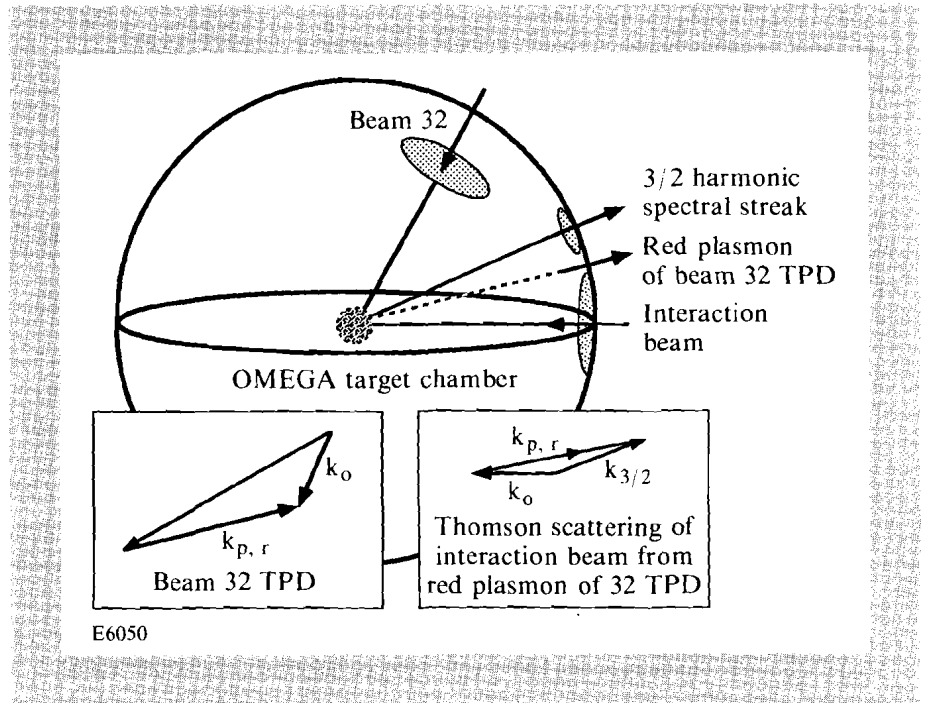
Figs. 51.1(b)–51.1(d), near $t \approx 1$ ns], or from the interaction beam (the strong, double-lobed signals on the right). In addition, an unusual red-shifted spectral component, which starts around 1.5 ns and lasts until about 1.7 ns, is observed in Figs. 51.1(b)–51.1(d). It is most easily seen in Figs. 51.1(c) and 51.1(d). In Fig. 51.1(d) this is the only feature related to the interaction beam since the interaction beam intensity was reduced to below the threshold for self-scattering, 3/2-harmonic generation. This signal disappears if either the secondary beams or the interaction beam is turned off. We have identified this red-shifted spectral component (hereafter referred to as the “probe-beam” feature) as being a result of Thomson scattering involving plasmons from the TPD instability of one of the secondary heating beams (OMEGA beam 32) and probe-beam photons from the interaction beam. A discussion of these two distinctive 3/2-harmonic features follows.

1. Probe-Beam Feature

The experimental geometry permitting observation of this spectral feature is shown schematically in Fig. 51.2 with the location of the interaction beam on the equator of the target chamber (east), the 3/2-harmonic observation port $\sim 20^\circ$ above (north) and in the plane of polarization of the interaction beam, and the secondary beam 32 located northeast at 50° latitude with its polarization pointing half-way between the interaction beam and the observation port. Beam 32 is the only one of the secondary beams that can produce “red” TPD plasmons with k -vectors that point roughly half-way between the interaction beam port and the 3/2-harmonic observation port. Furthermore, these plasmon k -vectors have the right length for 3/2-harmonic generation using a photon of the interaction beam. The corresponding k -vector diagrams are shown schematically in the boxes in Fig. 51.2. From calculations we find that these red plasmon k -vectors have $k_{p,r} \approx 2k_{o,vac}$, where $k_{o,vac}$ is the vacuum propagation vector of the $\lambda_o = 351$ -nm laser beam producing the TPD instability. The geometry and electron temperature determine uniquely the electron density at which the TPD occurs and the wavelength shift of this probe-beam feature relative to $2\lambda_o/3$.

Fig. 51.2

Schematic scattering diagram for probe-beam feature of 3/2-harmonic emission. Top part refers to target-chamber geometry; boxes show two-step scattering process for TPD decay of beam 32 and subsequent Thomson scattering involving the interaction beam. The vector $k_{3/2}$ points toward the observation port.



The density at which the corresponding TPD instability takes place is given by

$$n_e / n_c \approx 0.25 \left(1 + 3\kappa^2 \lambda_D^2 \right)^{-1}, \quad (1)$$

and the corresponding red shift of the probe-beam feature $\Delta\lambda_{3/2}$ can be calculated from

$$\Delta\lambda_{3/2} / \lambda_{3/2} \approx 0.5 (k_o \lambda_D) (\kappa \lambda_D) \cos \theta / \left(1 + 3\kappa^2 \lambda_D^2 \right), \quad (2)$$

where $\kappa = k_o/2 - k_{p,r}$ and $\cos\theta = \kappa \cdot k_o/(\kappa k_o) \approx 0.66$ are determined by the experimental geometry (Fig. 51.2). The electron Debye length is denoted by λ_D . Using $T_e \approx 1$ keV and κ as determined geometrically, we obtain from Eq. (1) $n_e \approx 0.23 n_c$, which is well above the Landau cutoff density of $0.2 n_c$ (see the following), and from Eq. (2) $\Delta\lambda_{3/2} \approx 12$ Å. This calculated wavelength shift agrees very well with the 10 Å to 11 Å measured in our experiments. The angle $\theta \approx 49^\circ$ is also very close to the optimum angle for the growth of the TPD instability.⁶

The probe-beam feature can be used advantageously to determine the TPD threshold during the falling part of the secondary heating beam (beam 32). The interaction beam, which acts here merely as a “probe” beam, increases steadily during the same period so that the disappearance of the Thomson signal corresponds to the disappearance of the TPD instability at that density. We can use this cutoff to obtain an upper limit to the experimental TPD threshold of $2\text{--}3 \times 10^{13}$ W/cm². This is approximately a factor of 2 below the usual linear gradient threshold¹⁰ of $\sim 5 \times 10^{13}$ W/cm². The instability could disappear either because the intensity of the secondary beam falls below the TPD threshold or because the plasma density falls below $0.23 n_c$. If the background density had actually fallen below $0.23 n_c$, our experimental threshold would clearly be an overestimate. The difference between the experimental and calculated thresholds may be a result of filamentation of beam 32 in the plasma, for which Epperlein¹¹ has estimated a threshold of $\sim 10^{13}$ W/cm². In contrast, use of the self-scattering threshold (the onset of the main 3/2-harmonic, double-lobed feature caused by the interaction beam in Fig. 51.1) would result in an inferred TPD threshold that is ten times higher than the probe-beam estimate given previously! The reason for this higher threshold lies in the complexity of the self-scattering signal, as will be discussed. Note that we do not see any evidence of self-scattering, 3/2-harmonic emission from the secondary heating beams alone.

2. Self-Scattering Feature

The main spectral features of the 3/2-harmonic emission are caused by self-scattering, with the interaction beam creating the TPD plasmons and then scattering off these plasmons. The measured spectral splitting of this feature is ~ 28 Å, with the red component shifted by $\sim +16$ Å relative to $2\lambda_o/3$ and the blue component shifted by ~ -12 Å. In addition, the red component is usually stronger than the blue component.

In principle, for high intensities the TPD instability should extend all the way to the Landau cutoff at $k_p\lambda_D \approx 0.3$, and indeed we require this to explain our experimental observations.¹² We can use Eq. (1) with $\kappa\lambda_D = 0.3$ to estimate the Landau cutoff density and obtain $n_e \approx 0.2 n_c$. The magnitude of each of the TPD plasma-wave k -vectors at this density is $\sim 3k_{o,vac}$. Ignoring the details of the scattering process leading to the self-scattering, 3/2-harmonic emission, one can obtain a splitting of the 3/2-harmonic spectrum by equating it to the frequency difference between the two TPD plasmons at the Landau cutoff. The corresponding wavelength shifts for the red and blue 3/2-harmonic spectral components are obtained from Eq. (2), using $\kappa\lambda_D = 0.3$ and $\theta \approx 45^\circ$, resulting in $\Delta\lambda_{3/2} \approx 17$ Å. This is in good agreement with the position of the red peak; but, as noted

previously, the shift of the blue peak is only about 12 Å. This smaller shift of the blue peak will be discussed further. Since the self-scattering, 3/2-harmonic spectra show a clear double-peak structure with little emission between the peaks, we conclude that this feature originates predominantly from the region near $0.2 n_c$, with little or no contribution from the TPD at higher densities.

A more fundamental problem is that the wave-vector matching conditions do not permit the combination of a laser photon with wave vector k_0 with a plasmon of wave vector $\sim 3k_0$ to produce a $3\omega_0/2$ photon with wave vector $\sim 3k_0/2$. One possible solution is to invoke weak turbulence: the plasmons decay repeatedly into ion-acoustic phonons and plasmons of shorter wave vector; after sufficient steps in this cascade their wave vectors are short enough to satisfy the matching conditions for $3\omega_0/2$ emission. Unfortunately, the cascade also reduces the frequencies of the plasmons, resulting in the average wavelength of the two $3\omega_0/2$ photons being shifted to the red by ~ 15 Å. This is much larger than the observed asymmetry and this explanation can therefore be ruled out.

Locally steep density gradients provide a means of relaxing the wave-vector matching conditions without changing the plasmon frequencies, since in steep gradients the wave vectors no longer have a precise value. One potential source of such gradients is strong turbulence, in which the plasmons become trapped in collapsing cavitons¹³ near $n_e \approx 0.2 n_c$. This model also accounts for the higher threshold of the self-scattering, 3/2-harmonic emission compared with the TPD instability since the energy density of the TPD plasma waves must rise to $\sim (k_p \lambda_D)^2 n_e k_B T_e$ before strong turbulence sets in. However, since the threshold for strong turbulence is lower for smaller plasmon wave vectors, and therefore at higher densities, this model does not explain why most of the self-scattering, 3/2-harmonic emission occurs at the Landau cutoff density, nor does it account for the asymmetry of the spectrum.

Another possibility is a sharp density gradient localized at the Landau cutoff density. Such a gradient could result from the rapid drop in plasmon ponderomotive pressure near the cutoff,^{14,15} the rapid drop in effective pressure would drive an increase in flow velocity and concomitant decrease in density near the cutoff. Besides explaining the preponderance of emission at the Landau cutoff, this model also naturally accounts for the asymmetry of the two peaks in wavelength and intensity: since the blue (higher-frequency) plasmons created by the TPD instability propagate *into* the plasma, they must undergo one ion-acoustic decay to reflect them back toward the cutoff. The frequency decrease ($2k_{p,b} c_s$) resulting from this decay is calculated to produce a wavelength shift of ~ 6 Å to the red for the resulting $3\omega_0/2$ light. Thus, the wavelength shift for the blue peak is reduced to ~ 11 Å, in good agreement with observation. The red plasmons, on the other hand, are created propagating outward and need undergo no reflection to reach the cutoff; thus the red peak remains shifted by 17 Å and retains its full intensity.

3. Influence of Beam-Smoothing Techniques on the 3/2-Harmonic Spectra

Figure 51.1(e) is an example of a time-resolved, 3/2-harmonic spectrum in the presence of SSD, which combines distributed phase plates, FM bandwidth, and angular dispersion. We note that the weak emission at the time of the primary

beams has disappeared as has the probe-beam feature around 1.5 ns. This implies that the TPD threshold as estimated from the probe-beam feature must have increased in these experiments by at least a factor of 2. Unfortunately, no data with variable intensity in beam 32 are currently available to establish a clear threshold. However, judging from intensity measurements made on time-integrated, self-scattering spectra using the interaction beam, we do not think that the threshold has increased by much more than a factor of 2. This can also be deduced—albeit with less accuracy—from the time-resolved data in Figs. 51.1(b) and 51.1(e). Doubling our original TPD threshold estimate based on the probe-beam feature brings it in very close agreement with the gradient threshold assuming 500- μm gradient scale lengths. (The theory for the TPD threshold in a parabolic density profile is not available at this time.)

At present we speculate that filamentation,¹¹ without SSD, sets in around 10^{13} W/cm². The enhanced intensity inside the filaments then reduces the apparent TPD threshold from that in the background plasma. Hydrodynamic arguments along with the optics of SSD suggest that a 10-GHz FM modulation with a bandwidth of $\Delta\lambda/\lambda \sim 3 \times 10^{-4}$ is sufficient to significantly reduce if not completely eliminate filamentation. Since the TPD threshold is not far above the filamentation threshold, the influence of filamentation on the overall TPD instability level well above threshold may not be very noticeable.

This speculation is supported by direct experimental evidence for filamentation found by Coe *et al.* in long-scale-length plasmas,¹⁶ and by indirect evidence in the same plasmas through stimulated Raman and Brillouin scattering by Willi *et al.*¹⁷ Using the same experimental techniques, this group reported both direct and indirect evidence for the suppression of filamentation when beam-smoothing techniques, such as induced spatial incoherence (ISI), were applied.^{18,19}

Peyser *et al.*²⁰ have reported significant reduction of 3/2-harmonic emission from laser plasmas when ISI beam-smoothing techniques were used. They have noted a fivefold increase in the TPD threshold for bandwidths of 5 Å to 10 Å at an interaction wavelength of 527 nm. They have attributed these observations partly to the suppression of filamentation and partly to direct bandwidth effects on the instability growth rates. However, in these experiments the same beam was used as the interaction beam and the plasma-producing beam, thus complicating the interpretation, since the plasma conditions change as the irradiation intensity changes. While we agree with their interpretation concerning suppression of filamentation, we see no evidence in our experimental results that the modest bandwidths applied in our case have any direct influence on reducing the 3/2-harmonic emission.

Further support for our filamentation hypothesis has been provided by two- and three-dimensional (2-D and 3-D) simulations by Schmitt,²¹ which clearly demonstrate the effect of ISI-type beam-smoothing techniques on the reduction or suppression of filamentation.

In all time-resolved, 3/2-harmonic spectra we note that the spectra end abruptly near 2.1 ns, independent of whether the interaction beam peaked

before or after this time (see Fig. 51.1). Comparing this observation with Fig. 51.1(f) we note that this corresponds to the time when the predicted peak on-axis density dips below $0.2 n_c$, the TPD Landau cutoff density. (The predictions for this time are insensitive to the timing of the interaction beam.) This may be taken as a confirmation of the interpretation that the self-scattering, 3/2-harmonic emission involves TPD decay near the Landau limit, i.e., at densities much closer to $0.2 n_c$ than $0.25 n_c$. Conversely, this observation is a confirmation of the predictive capability of the 2-D hydrodynamic code *SAGE*.

There is a further point of interest: the dip in the 3/2-harmonic emission near 1.8 ns, best observed in Fig. 51.1(e), corresponds very well with the excursion of the peak on-axis density below $0.2 n_c$ at the same time as predicted by *SAGE* and shown in Fig. 51.1(f). (The increase in the on-axis density at 2.0 ns is a result of mass flow toward the axis from the less-well-irradiated off-axis portion of the foil and is discussed in detail in Ref. 1.) The dip in the 3/2-harmonic emission is better seen in the blue component than in the much more intense red component, for which the streak record was very close to or beyond the saturation level. In the streaks without SSD this modulation may be washed out, either because of the generally high signal levels of the streak records or by complex interactions involving filamentation of the strongly modulated, stationary intensity distribution (speckle pattern). It should also be noted that this dip in density could affect our estimates of the TPD threshold on the basis of the probe-beam feature as was noted previously.

Amiranoff *et al.*²² and Basov *et al.*²³ have carried out 0.53- μm probe-beam experiments using solid targets irradiated at 1.064 μm at an intensity of $\sim 10^{15} \text{ W/cm}^2$. They were able to probe plasmons with k -vectors very close to the TPD Landau cutoff. While refraction of the various waves is certainly a significant problem for the interpretation of all of these experiments, Basov *et al.*²³ were able to deduce spectra of the plasma turbulence near $n_c/4$, which clearly extended to the Landau cutoff. Their results also indicated a drop in the turbulent plasma wave spectrum for $k_p \lambda_D \leq 0.13$, which the authors ascribe to density-scale-length effects. These probe-beam experiments are similar to the probe-beam experiments presented here, but they are relevant to the self-scattering regime because of the high intensities in the interaction beam. They also support our conclusions that the TPD instability extends all the way to its Landau cutoff.

Raman Spectrum

Raman scattering has been observed in many high-intensity, laser-produced plasmas.^{17, 24–27} The data presented here are both time integrated and time resolved and agree in many respects with observations elsewhere. However, on a number of points we come to significantly different conclusions, based on the combination of our Raman and 3/2-harmonic data and the data presented in Ref. 1.

Typical time-integrated Raman spectra are shown in Fig. 51.3 for the interaction beam peak timed at 1.6 and 2.2 ns. Compared with the spectra reported by Drake *et al.*,²⁵ these spectra are very narrow in spite of the fact that the interaction beam intensities are nominally comparable. The narrowness of

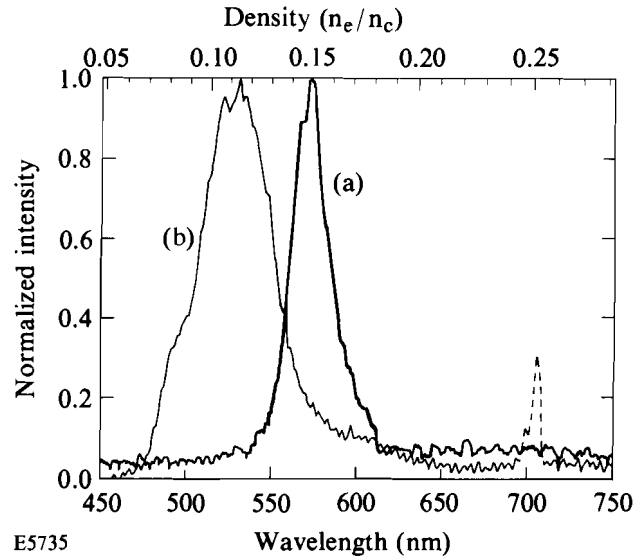


Fig. 51.3

Typical time-integrated Raman spectra obtained for two different timings of the interaction beam: (a) $t = 1.6$ ns, (b) $t = 2.2$ ns. Note: the 700-nm feature drawn dashed in (b) is caused by 3/2-harmonic emission from the 1054-nm tertiary heating beams that were on for this shot. (Any 1/2-harmonic emission from the 351-nm beams is fully reabsorbed by the plasma.)

our data indicates that the emission occurs over a small density range (see top scale in Fig. 51.3). In Ref. 1 we interpreted this as an indication that the Raman emission emanates from the maximum of the on-axis density profile, which is relatively stagnant around 1.6 ns while it decreases with time rather rapidly around 2.2 ns, in agreement with the wider Raman spectrum for this case.

The intensity dependence of the Raman emission at 45° to the backscatter direction shows a clear threshold near 2×10^{14} W/cm² with a linear growth region extending over nearly four orders of magnitude (see Fig. 51.4). Saturation appears to set in at an intensity only four times higher than the threshold. These data were all taken with the interaction beam peaking at 1.6 ns with all spectra closely resembling that of Fig. 51.3(a). The observed SRS threshold is actually very close to the collisional SRS threshold $I_{\text{Raman, coll}}$ in a parabolic density profile given by Williams²⁸ as

$$I_{\text{Raman, coll}} \approx 2.5 \times 10^{16} Z^{1/2} (n_e / n_c)^{1/4} / (T_{\text{keV}}^{3/2} \lambda_\mu^{3/2} L_\mu) \text{ W/cm}^2, \quad (3)$$

where Z is the average ionic charge, λ_μ is the laser wavelength in microns, and L_μ is the FWHM of the parabolic density profile $n_e/n_c = 1 - 2(x/L_\mu)^2$. For our experiments, with a typical value of $L_\mu \approx 500$ μm , Eq. (3) yields $I_{\text{Raman, coll}} \approx 2.5 \times 10^{14}$ W/cm².

Three typical time-resolved Raman spectra are shown in Figs. 51.5(a)–51.5(c) displayed on a common time axis with the interaction beam ($I_0 \sim 10^{15}$ W/cm²) peaking at 2.0, 2.4, and 2.6 ns, respectively. The background plasma was created in the same way in all cases, but the electron temperature evolution is expected to be different because of more (and earlier) heating caused by the interaction beam in the first case.¹ In all cases the Raman emission occurs early

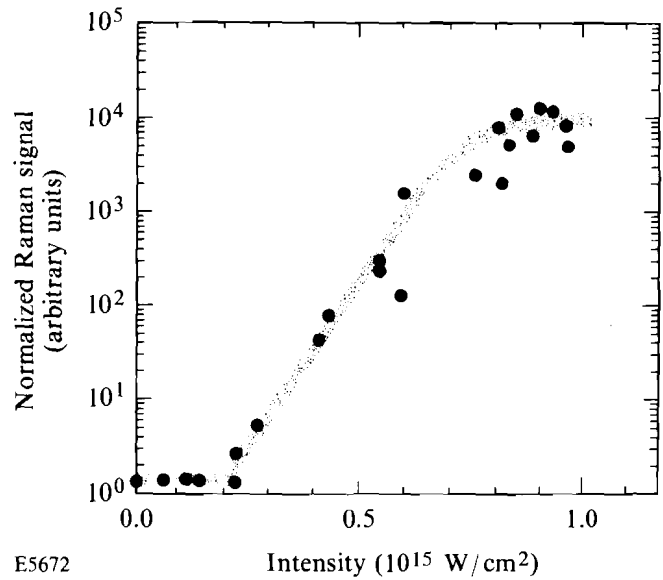


Fig. 51.4
Intensity dependence of the Raman emission for the peak of the interaction beam at $t = 1.6$ ns. These experiments used distributed phase plates on all beams but no applied FM bandwidth (no SSD).

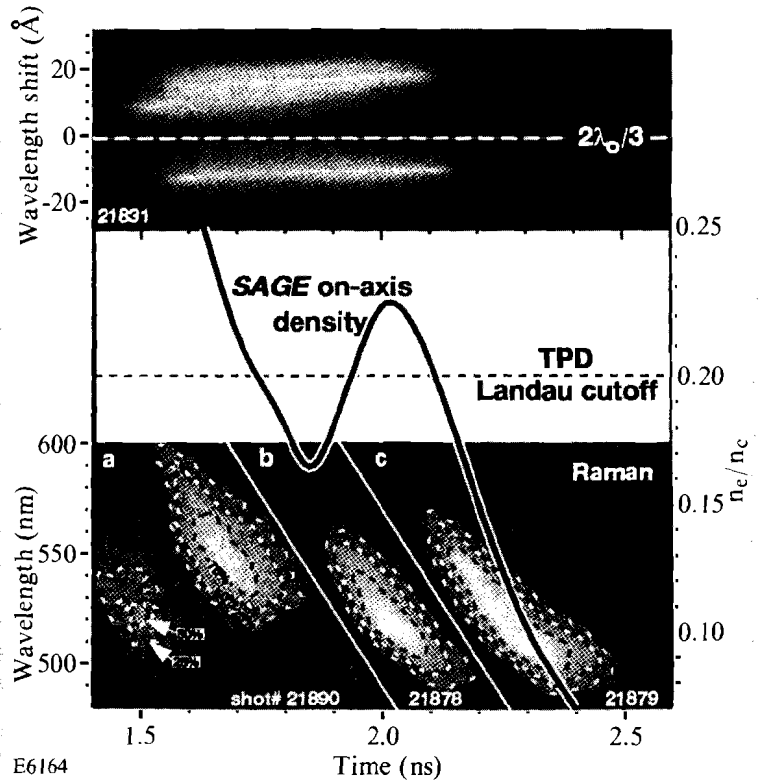


Fig. 51.5
Time-resolved Raman spectra for three shots without SSD and with the interaction beam of intensity $\sim 10^{15}$ W/cm² peaking at (a) 2 ns, (b) 2.4 ns, and (c) 2.6 ns. Tertiary heating beams were present in (a) but in none of the other shots. There is no additional structure beyond the straight white lines separating the different shots. Superposed on the streaks is the peak on-axis density evolution as calculated by SAGE in the absence of the interaction beam. The Landau cutoff (the late-time, short-wavelength cutoff) is indicative of the electron temperature $T_{keV} \approx 10 n_e/n_c$. A typical 3/2-harmonic streak for an interaction beam with its peak at 1.9 ns [see Fig. 51.1(b)] is shown on top for comparison.

during the interaction beam and ends well before its peak. Furthermore, the emission is observed at Raman wavelengths corresponding to densities well below $0.2 n_c$. It should be noted that Raman emission at $\lambda \geq 640$ nm (corresponding to emission at $n_e/n_c \geq 0.2$) typically suffers more than 75% absorption while propagating out through the plasma, whereas absorption below 550 nm is basically negligible. Observation of Raman emission from densities $>0.2 n_c$ is therefore unlikely. On the other hand, if the actual Raman emission (i.e., the emission before propagation through the plasma) had peaked above 640 nm, we should have seen more evidence for it, either in the time-resolved spectra taken at 45° or in the time-integrated spectra taken simultaneously at 0° (backscatter). We therefore conclude that the Raman emission occurred primarily at densities $<0.2 n_c$. This is consistent with numerous earlier experimental observations of what is often referred to as the “Raman gap” (little Raman signal between $\sim 0.2 n_c$ and $0.25 n_c$). There is no generally accepted explanation for this gap.

Comparing the time-resolved Raman spectrum in Fig. 51.5(c) with the peak density evolution obtained from the simulations [dotted curve of Fig. 7(b) of Ref. 1, also shown in Fig. 51.5], we find reasonable agreement between the two. The peak of the interaction beam ($\sim 10^{15}$ W/cm²) for this shot was very late, at 2.6 ns, at which time it is absorbed very weakly by the plasma. From Ref. 1 the perturbation to the plasma density profile caused by this interaction beam should be negligible. This spectrum suggests that the Raman emission shown in Fig. 51.5(c) originates from the peak of the density profile with the onset corresponding to the collisional threshold obtained from Eq. (3). The difference in detail ($\sim 20\%$) between the densities as determined from the Raman emission and predicted by *SAGE* is well within the predictive capability of such simulations and the less-than-perfect symmetry obtainable experimentally. Similar arguments probably account for the 3/2-harmonic emission near 1.9 ns not ceasing as expected (the predicted density dips below $0.2 n_c$), although shots with beam smoothing show some indications of the existence of this dip [Fig. 51.1(e)].

The short-wavelength (low-density) cutoff observed at later times is consistent with Landau damping of the Raman plasma waves. This cutoff wavelength can be used as a temperature diagnostic;^{29,30} from $k_p \lambda_D \approx 0.3$ and the dispersion relations we find $T_{\text{keV}} \approx 10 n_e/n_c$ for cutoff densities near or below $0.1 n_c$. The temperature thus determined (~ 1 keV at $n_e/n_c \approx 0.08$) is consistent with the temperatures found in Fig. 7 of Ref. 1 at 2.3 to 2.5 ns.

In contrast, the temporal evolution of the Raman spectra shown in Fig. 51.5(a) and 51.5(b) does not agree so well with the predicted evolution of the peak density. For these shots the interaction beam peaked at 2.0 and 2.4 ns, respectively. The narrowness of the instantaneous Raman spectra indicates that, instantaneously, most of the emission occurs in a very narrow density region that rapidly decreases toward lower densities down to the Raman Landau cutoff. In Fig. 51.5(a) the temperature inferred from the Raman Landau cutoff (~ 1.3 keV at $n_e/n_c \approx 0.13$) is a little higher than that in Fig. 51.5(c), again consistent with the simulations showing higher temperatures at earlier times.

At present there is no very convincing explanation for the observed temporal evolution of the Raman spectra at early times, when the peak density is $>0.2 n_c$

as expected from simulations and apparently confirmed by the 3/2-harmonic spectra shown in Fig. 51.1 and on top of Fig. 51.5. The observed temporal evolution of these Raman spectra indicates that the emission takes place at a density that decreases much more rapidly than the peak density in the hydrodynamic simulations. The calculated density history with the interaction beam at 2.0 ns [as for Fig. 51.5(a)] is slightly lower than the solid curve of Fig. 51.5, but not enough to match the Raman emission of Fig. 51.5(a). It is possible that the code may underestimate the extent to which the interaction beam perturbs the preformed plasma. With a 2-D density profile that has a minimum on axis (such as happens up to ~ 1.8 ns according to Fig. 12 of Ref. 1) one could obtain simultaneous Raman emission at $0.15 n_c$ from the axis and $3\omega/2$ emission at 0.20 to $0.25 n_c$ off-axis, with both emissions coming from the central portion of the plasma. However, a number of alternative explanations should also be considered, such as filamentation or self-focusing, profile steepening near $0.2 n_c$, or the bump-on-tail instability. Direct evidence of Raman scattering from filaments has been reported by Willi *et al.*¹⁹ and indirect evidence has been widely reported.^{17,18,31,32} Alternatively, profile steepening^{14,15} in the vicinity of the TPD Landau cutoff at $0.2 n_c$, with the drop increasing in time, could also account for our observed Raman spectra. Finally, similar spectra could be explained by enhanced Thomson scattering³³ driven by pulses of fast electrons that excite bump-on-tail plasmons. These electrons would have their origin in the vigorous TPD instability above $0.2 n_c$, and the fall of Raman wavelength in time would be explained by a decrease in directed energy of the fast-electron pulses as the plasma length increases. One should also note the interesting feature in the bottom-left portion of Fig. 51.5(a), corresponding to Raman emission from a low density at an early time. Similar features have been seen on other streaked spectra taken during the early phases of the expanding plasma.

Independent of the model used, the simultaneous emission of the 3/2 harmonic (TPD at densities $\geq 0.2 n_c$) and Raman scattering from densities below $0.2 n_c$ clearly indicates that the long-wavelength cutoff of the Raman spectra does not necessarily provide a reliable measure of the peak on-axis density evolution. This is in marked contrast to the general understanding that Raman spectra can be used as diagnostics of the peak density.^{17,25,34}

It should also be noted that the onset of the Raman spectra coincides with the onset of the TPD self-scattering signal, which may indicate a relationship between the two processes. Such a relationship has been postulated previously by Simon and Short.^{33,35} The strongly driven TPD instability leads to caviton collapse and the generation of pulses of fast electrons. The observed Raman spectra could then be a result of enhanced Raman scattering from plasma waves created lower in the density gradient by these electrons. However, this model would not apply to the Raman emission of Fig. 51.5(c) that occurs at times (>2.1 ns) beyond which no 3/2-harmonic emission is seen (Fig. 51.1) and for which *SAGE* predicts peak densities $<0.2 n_c$.

The sensitivity of the Raman emission to the SSD beam-smoothing technique is shown in Fig. 51.6, where a modest bandwidth of $\Delta\lambda/\lambda = 3 \times 10^{-4}$ is shown to

lead to a reduction in the Raman signal by three orders of magnitude. A similarly dramatic reduction in Raman scattering was observed by Obenschain *et al.*³¹ in $\lambda = 1.054\text{-}\mu\text{m}$, solid-target irradiation experiments using ISI ($\Delta\lambda/\lambda = 1.5 \times 10^{-3}$). However, a detailed comparison of these experiments with our results is difficult because of the very different nature of the plasma, very different scale lengths, and different irradiation wavelengths. In long-scale-length, 527-nm-irradiation experiments at Rutherford, Willi *et al.*¹⁹ have also observed significantly reduced Raman emission, although less dramatic than in the experiments reported here. Unfortunately, their irradiation intensities were limited to values below the SRS threshold in the presence of ISI. In both of these reports it was noted that reduction or suppression of filamentation caused by the ISI beam-smoothing technique is likely the primary reason for the reduced SRS signal strengths, rather than direct reduction of the SRS growth rates³⁶ caused by the applied bandwidth. Similarly, any modification of the collapse process by SSD might also decrease the hot-electron emission and thus decrease any enhanced Raman scattering.

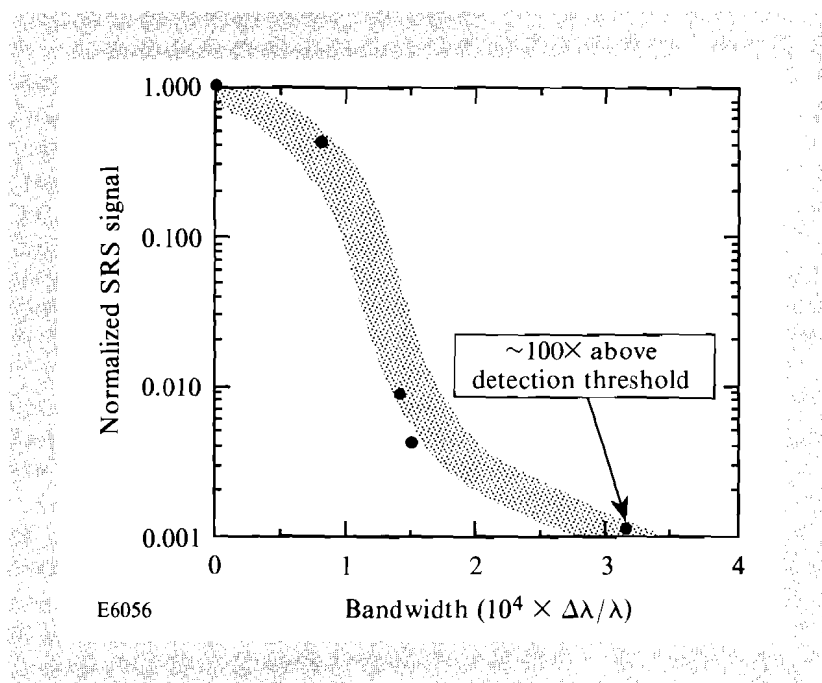


Fig. 51.6

Dependence of Raman signal on applied FM bandwidth for smoothing by spectral dispersion (SSD). The interaction-beam intensity is $\sim 10^{15}$ W/cm² and its peak is at 1.6 ns. The background plasma conditions are the same as for Fig. 51.4.

Alternatively, only a small increase in the Raman threshold (by a factor of 2 or 3) would be necessary to account for the observed decrease in Raman emission. Time-resolved Raman spectra with SSD (not presented here) are typically delayed by 100 to 200 ps relative to the Raman spectra without bandwidth. This time delay corresponds approximately to a two-times-higher laser pulse intensity at the onset of the Raman emission in the presence of SSD. A more accurate determination of the Raman threshold with SSD requires further experiments.

If the Raman emission were to occur on a density shelf resulting from profile steepening by the TPD instability, the threshold for Raman scattering would be

determined by the intensity required to produce a significant nonlinear level of TPD plasma waves, which should correspond roughly to the threshold for the TPD self-scattering. This is consistent with the non-SSD observations of the two thresholds (i.e., Raman and 3/2-harmonic self-scattering). However, the level of TPD plasma waves would determine the density of the shelf and would have to vary in such a way as to match the temporal fall-off of the Raman density in Fig. 51.5. The absence of strongly driven TPD during the late-time Raman emission of Fig. 51.5(c) indicates that neither the fast-electron model nor the density-shelf model may be applicable in this case.

Discussion

One notable result of this investigation is the apparent interconnection between the TPD and the Raman spectra. The time-resolved Raman data appear to indicate that in the presence of densities $>0.2 n_c$ the Raman emission originates in regions of lower density. It is therefore possible that the presence of the TPD instability at $>0.2 n_c$ excludes the Raman instability, perhaps through enhanced ion fluctuations, which are invariably observed to accompany the TPD instability.³⁷ Such enhanced ion fluctuations³⁸ have indeed been observed to suppress Raman scattering so that this conjecture would be self-consistent. The apparent preponderance of large- k_p plasmons may be related to the disappearance of the quarter-critical surface at $t \approx 1.5$ ns. For later times, the density hovers relatively close to the Landau cutoff density (see Fig. 51.5).

The apparent saturation observed at the highest intensities in Fig. 51.4 is probably a result of the rapid temporal evolution of the Raman spectra to the Landau cutoff rather than to any linear or nonlinear saturation effect. The time-resolved Raman spectra (Fig. 51.5) appear to furnish a possible explanation for this saturation. Since the SRS emission threshold lies near 2×10^{14} W/cm² and the Raman emission region drops in density rapidly to its Landau cutoff density, increasing the interaction beam intensity beyond a certain value will simply shift the Raman onset and cutoff toward earlier times without significantly changing the total Raman emission.

The strong decrease in Raman signal upon application of SSD bandwidth is consistent with observations elsewhere and is compatible with the inferred interconnection between the TPD and the Raman instabilities. Thus, the TPD instability would be only modestly affected by SSD through a two- to four-fold increase in its threshold, perhaps as a consequence of reduced filamentation, and hence reduced peak pump intensity driving the TPD instability. The same increase in the SRS threshold would lead to a very marked reduction in Raman signal because of its strong intensity scaling (see Fig. 51.4). Again, we note the alternative possibility that SSD can modify the Langmuir collapse of the TPD plasmons, leading to reduced fast-electron emission and a lower level of enhanced Raman scattering.

Our basic observations relating to the sensitivity of the TPD and SRS instabilities to SSD (or ISI) beam-smoothing techniques are consistent with observations made elsewhere at different wavelengths and under different plasma conditions.^{17-20,31} However, the apparent interconnection between the

TPD and SRS instabilities has not been found in these references, possibly because no simultaneous 3/2-harmonic and Raman measurements were made.

Summary

We have successfully used the flexibility afforded by the multiple-beam OMEGA system to generate hot, long-scale-length plasmas and to study parametric instabilities at and below $n_c/4$ at an irradiation wavelength of 351 nm. The data indicate that the TPD instability extends all the way to its Landau cutoff at $n_e \approx 0.2 n_c$. We have further shown that this instability is only modestly affected by beam-smoothing techniques such as SSD. It is possible that this last effect is a result of reduced filamentation of the interaction beam in the preformed plasma.

We have no evidence in our experiments that the Raman emission occurs at densities $\geq 0.2 n_c$. In fact, it is observed only well below the TPD Landau cutoff density, typically at $n_e \leq 0.16 n_c$. Furthermore, this emission rapidly chirps down to lower density (shorter wavelengths) until it reaches its Landau cutoff density, which can be used as an electron temperature diagnostic. Estimates of the latter agree with temperatures predicted by *SAGE*. Further, the Raman emission is strongly reduced upon the introduction of SSD. We have proposed a number of possible explanations for these observations but further experiments will be required to clarify remaining ambiguities.

ACKNOWLEDGMENT

The authors would like to thank the OMEGA operations group for their expert help in carrying out the complex experiments reported here. Special thanks are also owed to S. Noyes for fabricating the targets and to the experimental plasma physics group at Lawrence Livermore National Laboratory for the loan of the streak camera whose data were most essential to the success of the experiments reported here.

This work was supported by the U.S. Department of Energy Office of Inertial Confinement Fusion under agreement No. DE-FC03-85DP40200 and by the Laser Fusion Feasibility Project at the Laboratory for Laser Energetics, which is sponsored by the New York State Energy Research and Development Authority and the University of Rochester.

REFERENCES

1. W. Seka, R. S. Craxton, R. E. Bahr, D. L. Brown, D. K. Bradley, P. A. Jaanimagi, B. Yaakobi, and R. Epstein, *Phys. Fluids B* **4**, 432 (1992).
2. Y. Kato *et al.*, *Phys. Rev. Lett.* **53**, 1057 (1984).
3. See National Technical Information Service Document No. DOE/DP40200-65 [LLE Review **33**, 1 (1987)]. Copies may be ordered from the National Technical Information Service, Springfield, VA, 22161.
4. S. Skupsky, R. W. Short, T. Kessler, R. S. Craxton, S. Letzring, and J. M. Soures, *J. Appl. Phys.* **66**, 3456 (1989).
5. C. S. Liu and M. N. Rosenbluth, *Phys. Fluids* **19**, 967 (1976).
6. A. Simon, R. W. Short, E. A. Williams, and T. Dewandre, *Phys. Fluids* **26**, 3107 (1983).
7. J. L. Bobin *et al.*, *Phys. Rev. Lett.* **30**, 594 (1973); P. Lee *et al.*, *Appl. Phys. Lett.* **24**, 406 (1974); H. C. Pant *et al.*, *Opt. Commun.* **16**, 396 (1976).

8. A. I. Avrov *et al.*, *Sov. Phys. JETP* **43**, 507 (1977); V. Yu. Bychenkov *et al.*, *Beitr. Plasmaphys.* **23**, 331 (1983); R. L. Berger and L. V. Powers, *Phys. Fluids* **28**, 2895 (1985).
9. W. Seka, B. B. Afeyan, R. Boni, L. M. Goldman, R. W. Short, and K. Tanaka, *Phys. Fluids* **28**, 2570 (1985).
10. W. L. Kruer, *The Physics of Laser Plasma Interactions* (Addison-Wesley, Redwood City, CA, 1988), p. 83.
11. E. M. Epperlein, *Phys. Rev. Lett.* **65**, 2145 (1990); E. M. Epperlein and R. W. Short, submitted for publication to *Phys. Fluids B*. (APS-DPP 1991 invited talk).
12. Similar assumptions have been made by S. J. Karttunen, *Laser Part. Beams* **3**, 157 (1985); however, Karttunen's analysis does not lead to agreement with our observations.
13. A. M. Rubenchik and V. E. Zakharov, in *Handbook of Plasma Physics*, edited by M. N. Rosenbluth and R. Z. Sagdeev (Elsevier Science Publishers, New York, 1991), Vol. 3, p. 335; R. Z. Sagdeev *et al.*, *Sov. Phys. JETP* **55**, 74 (1982).
14. H. A. Baldis, J. C. Samson, and P. B. Corkum, *Phys. Rev. Lett.* **41**, 1719 (1978).
15. A. B. Langdon, B. F. Lasinski, and W. L. Kruer, *Phys. Rev. Lett.* **43**, 133 (1979).
16. S. E. Coe, T. Afshar-rad, and O. Willi, *Opt. Commun.* **73**, 299 (1989).
17. O. Willi *et al.*, *Opt. Commun.* **70**, 487 (1989).
18. S. E. Coe *et al.*, *Europhys. Lett.* **10**, 31 (1989).
19. O. Willi *et al.*, *Phys. Fluids B* **2**, 1318 (1990).
20. T. A. Peyser *et al.*, *Phys. Fluids B* **3**, 1479 (1991).
21. A. J. Schmitt, *Phys. Fluids* **31**, 3079 (1988); A. J. Schmitt, *Phys. Fluids B* **3**, 186 (1991).
22. F. Amiranoff *et al.*, *Bull. Am. Phys. Soc.* **30**, 1528 (1985).
23. N. G. Basov *et al.*, in *Proceedings on Basic and Advanced Diagnostic Techniques for Fusion Plasmas*, Varenna, Italy, 1986, edited by P. E. Stott *et al.* (Commission of European Communities, Directorate General XII, Brussels, 1986), Vol. 3, p. 997; and N. G. Basov *et al.*, *Phys. Lett.* **77A**, 163 (1980).
24. K. Tanaka, L. M. Goldman, W. Seka, M. C. Richardson, J. M. Soures, and E. A. Williams, *Phys. Rev. Lett.* **48**, 1179 (1982).
25. R. P. Drake *et al.*, *Phys. Fluids B* **1**, 2217 (1989); R. P. Drake *et al.*, *Phys. Fluids B* **1**, 1089 (1989); R. P. Drake *et al.*, *Phys. Fluids* **31**, 1795 (1988); R. P. Drake *et al.*, *Phys. Rev. Lett.* **60**, 1018 (1988).
26. A. V. Kil'pio *et al.*, *Sov. J. Quantum Electron.* **20**, 536 (1990).

27. C. Labaune *et al.*, Phys. Fluids B **2**, 166 (1990).
28. E. A. Williams, see National Technical Information Service Document No. DE87011009 [Lawrence Livermore National Laboratory Laser Program Annual Report (1985)].
29. W. Seka, E. A. Williams, R. S. Craxton, L. M. Goldman, R. W. Short, and K. Tanaka, Phys. Fluids **27**, 2181 (1984).
30. B. La Fontaine *et al.*, Bull. Am. Phys. Soc. **36**, 2351 (1991).
31. S. P. Obenschain *et al.*, Phys. Rev. Lett. **62**, 768 (1989).
32. R. W. Short, W. Seka, and R. Bahr, Phys. Fluids **30**, 3245 (1987).
33. A. Simon and R. W. Short, Phys. Rev. Lett. **53**, 1912 (1984).
34. S. E. Coe, T. Afshar-rad, D. Bassett, J. Edwards, and O. Willi, Opt. Commun. **81**, 47 (1991).
35. S. H. Batha, R. Bahr, L. M. Goldman, W. Seka, and A. Simon, Phys. Fluids **31**, 3667 (1988); S. H. Batha, D. D. Meyerhofer, A. Simon, and R. P. Drake, Phys. Fluids. B **3**, 448 (1991).
36. P. N. Guzdar *et al.*, Phys. Fluids B **3**, 776 (1991).
37. H. A. Baldis and C. J. Walsh, Phys. Fluids **26**, 1364 (1983).
38. H. A. Baldis *et al.*, Phys. Fluids B **3**, 2341 (1991).

1.B Thermal Stimulated Brillouin Scattering

An electromagnetic wave propagating through a plasma can be scattered by an ion-acoustic wave, transferring energy to the sound wave and the scattered light wave in such a way that these waves grow exponentially in time. This instability, known as stimulated Brillouin scattering (SBS), is a potentially serious energy-loss mechanism for laser-driven fusion and so has been studied extensively both experimentally¹⁻³ and theoretically.⁴⁻⁶ Previous theoretical analyses of SBS in laser-produced plasmas have generally proceeded on the assumption that the plasma is isothermal; this assumption is justified because the wavelength of the sound wave is very small (about half the laser wavelength), so that using classical (Spitzer-Härm⁷) thermal-transport theory the time for thermal equilibration across this distance is found to be much smaller than the sound-wave period. In this model the driving term for the instability is the ponderomotive force: plasma tends to be driven out of regions of high electromagnetic field intensity arising from the interference between the incident and scattered light waves, so that the interference pattern intensifies the sound wave.

Recently, however, numerical studies of thermal transport in laser-fusion plasmas using the Fokker-Planck (F-P) equation have shown that classical transport theory is inadequate to treat phenomena occurring over short distances, even if the local temperature scale length ($T/|\nabla T|$) is much longer than the

electron mean free path.^{8,9} In particular, it is found that thermal conduction can be greatly reduced for temperature variations with wavelengths shorter than the mean free path of the electrons that classically carry the bulk of the heat flow. These electrons, which have velocities near $3.7 v_t$ (where v_t is the electron thermal velocity), rapidly become uniformly distributed and decoupled from the spatial variations in energy density that persist in the slower electrons, which contain most of the thermal energy. Thus these spatial variations persist longer than predicted by classical theory. This effect is especially significant if the energy variations arise from a source that preferentially heats the slower electrons.⁹ Inverse bremsstrahlung, the principal heating mechanism in laser-produced plasmas, is such a source, since it arises from thermalization of the electron oscillatory velocity by collisions with ions, which are more frequent for slow electrons.

Since SBS involves ion waves with very short wavelengths, these advances in the understanding of thermal transport make it necessary to question the isothermality assumption in SBS theory. Inverse-bremsstrahlung heating raises the temperature and pressure of the plasma in regions of high electromagnetic field intensity and thus tends to expel plasma from such regions just as the ponderomotive force does. With classical thermal conductivity the resulting temperature variations would be negligible, but in the light of the 'nonlocal' transport theory previously described we shall find that they are significant, and in high-Z plasmas they can in fact become the dominant driving force for the SBS instability. We note in passing that a similar mechanism has been proposed in the analysis of SBS in ionospheric heating experiments;¹⁰ in that case it is the Earth's magnetic field rather than nonlocal transport effects that provides the necessary reduction in thermal transport.

To analyze the instability we consider a homogeneous equilibrium plasma with electron density n_0 and temperature T_0 . The electric field of the laser light is represented by $E = E_0 \exp[i(k_0 x - \omega_0 t)] + c. c.$, where $\omega_0^2 = \omega_p^2 + k_0^2 c^2$ and ω_p is the electron plasma frequency. For simplicity we consider only backscatter, so that the scattered light field can be represented by $E_1(t) \exp[i(k_1 x - \omega_1 t)] + c. c.$, the temperature perturbation by $T_1(t) \exp[i(kx - \omega t)] + c. c.$, and the density perturbation by $n_1(t) \exp[i(kx - \omega t)] + c. c.$, where $\omega_1^2 = \omega_p^2 + k_1^2 c^2$, $k_1 = k_0 - k$, $\omega = \omega_0 - \omega_1$, c_s is the ion sound speed, and k is the wave number of the ion sound wave. We assume perfect wave-number matching and look for temporal growth, represented by the slow time dependence of E_1 , T_1 , and n_1 . Using Maxwell's equations and the usual fluid equations for the plasma the derivation of the equations for the perturbed fields and densities is straightforward:

$$2i\omega_1 \frac{\partial}{\partial t} E_1^*(t) = -\frac{\omega_1}{\omega_0} \omega_p^2 E_0^* \frac{n_1(t)}{n_0}, \quad (1)$$

$$\left[\omega^2 - k^2 c_s^2 + 2i\omega \frac{\partial}{\partial t} - \frac{\partial^2}{\partial t^2} \right] \frac{n_1(t)}{n_0} = k^2 c_s^2 \frac{T_1(t)}{T_0} + \frac{Ze^2}{m_e m_i \omega_0 \omega_1} k^2 E_0 E_1^*(t) \quad (2)$$

Here, c is the speed of light, Z is the average ion charge, and m_e and m_i are the electron and ion masses.

There are two potential sources of energy that can drive the temperature variation T_1 : the PdV work of the oscillating sound wave and the inverse-bremsstrahlung heating resulting from the light waves. From F-P simulations we have found that the former, which adds energy to all electron velocity groups equally, is smoothed so rapidly by thermal conduction that it makes a negligible contribution to the temperature variation. In contrast, inverse bremsstrahlung heats mainly the slow electrons, and the resulting variations in energy density are smoothed much less rapidly than classical models would predict. Balancing inverse-bremsstrahlung heating with thermal diffusion and taking into account the temperature and density dependence of the inverse-bremsstrahlung absorption coefficient we find the following expression for the temperature variation:

$$\left\{ \frac{3}{2} \left[\frac{\partial}{\partial t} - i\omega \right] + \frac{\kappa_o^{\text{Th}} k^2}{n_o} + \frac{3}{2} \frac{\kappa_o^{\text{IB}} I_o}{n_o T_o} \right\} \frac{T_1(t)}{T_o} = \frac{2}{n_o T_o} \frac{\kappa_o^{\text{IB}} I_o}{n_o} \frac{n_1(t)}{n_o} + \frac{c \sqrt{\epsilon_o} \kappa_o^{\text{IB}}}{2 \pi n_o T_o} E_o E_1^*(t). \quad (3)$$

Here, ϵ_o is the homogeneous plasma dielectric constant, κ_o^{IB} is the inverse-bremsstrahlung absorption coefficient, I_o is the incident laser intensity, and κ_o^{Th} is the modified thermal conductivity to be discussed. In Eqs. (1)–(3) we have for simplicity neglected the various wave-damping mechanisms. It would be possible to include damping in the usual phenomenological way¹¹ by the replacement $\omega \rightarrow \omega + i\nu$ in Eqs. (1) and (2), where ν would be the inverse-bremsstrahlung damping rate for the light wave in Eq. (1) and a combination of collisional and Landau damping for the sound wave in Eq. (2). A more sophisticated approach would be to write an additional energy equation for the PdV work with the conductivity and specific heat modified to model both collisional and kinetic damping.¹² We will not pursue this subject further here since we are primarily interested in determining under what circumstances the thermal driving term significantly enhances the SBS growth rate, and this question is to first order independent of damping. A simple way to estimate the instability threshold as a result of damping will be discussed.

The terms in Eqs. (1)–(3) involving κ_o^{IB} , κ_o^{Th} and the electric fields may be conveniently written in terms of dimensionless parameters γ_{T1} , γ_{T2} , and γ_p (closely related to those introduced by Schmitt¹³):

$$\frac{\kappa_o^{\text{IB}} I_o}{\omega n_o T_o} = \frac{3}{2} \frac{\gamma_{T2}}{\gamma_{T1}},$$

$$\frac{\kappa_o^{\text{Th}} k^2}{\omega n_o} = \frac{3}{2} \frac{1}{\gamma_{T1}} \frac{\kappa_o^{\text{Th}}}{\kappa_o^{\text{SH}}},$$

where γ_{T1} is the ratio of the thermal-conduction transit time to the ion-acoustic transit time across k^{-1} ($\approx c / 2\omega_0 \sqrt{\epsilon_0}$),

$$\gamma_{T1} = 6.75 \times 10^{-6} \frac{\ln \Lambda}{T_0^2 (\text{keV}) \sqrt{\epsilon_0} \lambda_0 (\mu\text{m})} \frac{Z^*}{\phi(Z^*)} \left(\frac{Z}{A} \right)^{1/2} \left(\frac{n_0}{n_c} \right), \quad (4)$$

γ_{T2} is the ratio of the inverse-bremsstrahlung heating rate to the thermal-conduction cooling rate across k^{-1} ,

$$\gamma_{T2} = 2.24 \times 10^{-9} \frac{I_0 (10^{14} \text{ W/cm}^2)}{T_0^5 (\text{keV}) \epsilon_0^{3/2}} \frac{Z^{*2} (\ln \Lambda)^2}{\phi(Z^*)} \left(\frac{n_0}{n_c} \right)^2, \quad (5)$$

γ_p and γ_p is the ratio of the ponderomotive pressure to the thermal pressure:

$$\gamma_p = \frac{e^2 E_0 E_0^*}{m_e \omega_0^2 T_0} = 9.33 \times 10^{-3} \frac{\lambda_0^2 (\mu\text{m}) I_0 (10^{14} \text{ W/cm}^2)}{\sqrt{\epsilon_0} T_0 (\text{keV})}. \quad (6)$$

In these expressions A is the ion atomic number, $Z^* \equiv \langle Z^2 \rangle / \langle Z \rangle$ (where $\langle \rangle$ denotes an average over the ion species), $\phi(Z^*) \equiv (Z^* + 0.24) / (1 + 0.24 Z^*)$, and $\ln \Lambda$ is the Coulomb logarithm.

The factor $\kappa_0^{\text{Th}} / \kappa_0^{\text{SH}}$ represents the ratio of the thermal conductivity for inverse-bremsstrahlung heat to the classical Spitzer-Härm conductivity. It has been shown previously by means of F-P simulations⁹ that the effects of nonlocal transport on thermal conductivity for the case of an inverse-bremsstrahlung heating perturbation of wave number k are very well approximated by

$$\left(\frac{\kappa_0^{\text{Th}}}{\kappa_0^{\text{SH}}} \right) = \frac{1}{1 + (\alpha k \lambda_e)^\beta}, \quad (7)$$

where $\lambda_e \equiv T_0^2 / 4\pi n_0 e^4 \left[4.2 Z^* / \phi(Z^*) \right]^{1/2} \ln \Lambda$. The parameters α and β are chosen to fit the numerical results as described in Ref. 9; for the conditions relevant to SBS, i.e., $10 \leq k \lambda_e \leq 1000$, simulations show that the best fit is given by $\alpha \approx 21$ and $\beta \approx 1.44$. (The effects of ion motion and time-varying heating were included in these simulations but had no significant effect on the values of $\kappa_0^{\text{Th}} / \kappa_0^{\text{SH}}$.) Assuming a time dependence for the perturbed quantities of the form $\exp(-i\Omega t)$ and using the thermal-conductivity correction factor (7), Eqs. (1)–(3) become simultaneous algebraic equations that may be combined to yield the dispersion relation for the instability as a quartic polynomial in Ω . The roots are readily found numerically and the imaginary part corresponds to the instability growth rate (generally only one root has a positive imaginary part). The growth rates are maximized for values of k near the resonance of the scattered electromagnetic wave

$$k = 2k_0 - \frac{2\omega_0}{c} \frac{c_s}{c}$$

and this value of k is used in obtaining the following results.

For low- Z plasmas it is found that nonlocal thermal conductivity has a negligible effect, and the ponderomotive force remains the dominant driver for SBS. However, for high- Z plasmas, which provide the x rays in radiatively driven laser-fusion targets,¹⁴ the inverse-bremsstrahlung heating becomes significant. Figure 51.7 shows the growth rate $\text{Im}(\Omega)$ as a function of laser intensity for an Au ($Z=70$) plasma with $n_0/n_c=0.5$ and $T_0=1$ keV. The classical (isothermal) ponderomotive result is shown by the dashed curve. The solid curve results from Eqs. (1)–(3) and Eq. (7) and shows an enhancement of more than a factor of 2 throughout the intensity range. The enhancement of growth arises from thermally driven SBS, which dominates when $(\kappa_0^{\text{Th}}/\kappa_0^{\text{SH}})^{-1}\gamma_{T2}/\gamma_p > 1$. As a check on the fluid model results, F-P simulations were run at selected values of the intensity, shown by the circles in Fig. 51.7. The agreement is quite good at all intensities, with the fluid model slightly underestimating the growth-rate enhancement.

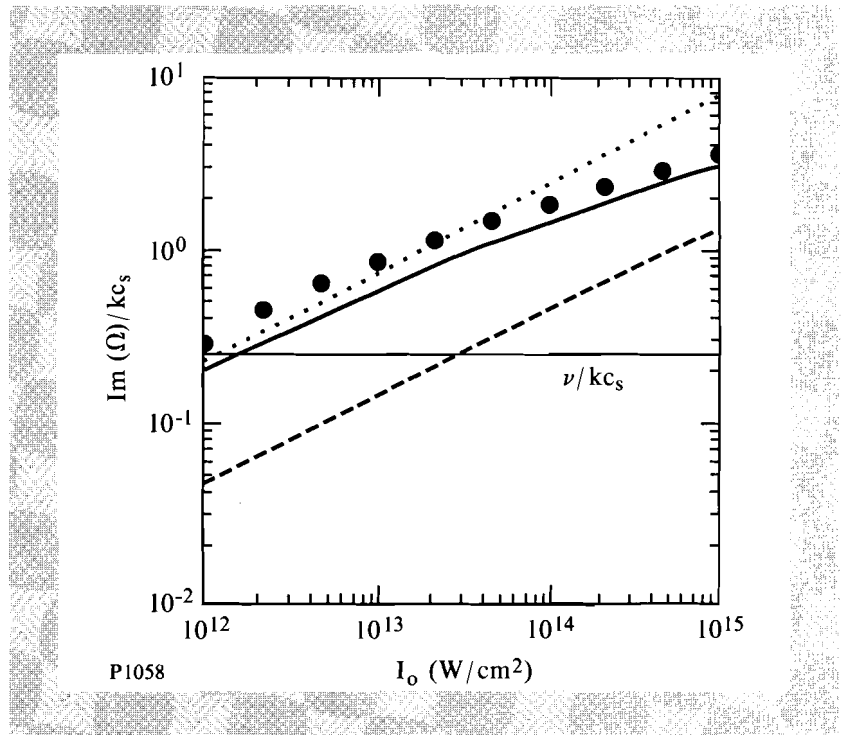


Fig. 51.7. Growth rates of SBS normalized to kc_s as a function of the incident laser intensity for a gold ($Z=70$) plasma with $n_0/n_c=0.5$, $T_0=1$ keV. The dashed line corresponds to the classical isothermal ponderomotive result, the solid line represents the growth rates calculated from Eqs. (1)–(3) and Eq. (7), the solid circles show the results of Fokker-Planck simulations, and the dotted line is the approximate growth rate given by Eq. (9). The horizontal line represents the homogeneous threshold due to damping as given by Eq. (8).

In a homogeneous plasma the threshold for instability is determined by the damping rates for the daughter waves:

$$\text{Im}(\Omega) > \nu \equiv \sqrt{\nu_{\text{EM}}\nu_{\text{IA}}} \quad (8)$$

where ν_{EM} is the inverse-bremsstrahlung damping rate for the scattered-light wave and ν_{IA} is the damping rate for the ion-acoustic wave. The ion-acoustic

wave damping is primarily electron Landau damping for high- Z plasmas with $ZT_e > T_i$.¹⁵ The inverse-bremsstrahlung damping of the scattered light is given by $\nu_{EM} = n_o \nu_{ei} / 2n_c$, where ν_{ei} is the electron-ion collision frequency.¹⁶

The horizontal line in Fig. 51.7 indicates the threshold for SBS resulting from Eq. (8). Note that the threshold intensity is lowered by nearly two orders of magnitude by thermal effects.

At low intensities, γ_{T2} and γ_p become small enough that the dispersion relation resulting from Eqs. (1)–(3) and Eq. (7) may be considerably simplified. The resulting approximate expression for the growth rate $G = \text{Im}(\Omega)$ is

$$\frac{\Gamma^2}{k^2 c_s^2} = \frac{1}{8} \frac{n_o}{n_c} \frac{c}{c_s} \frac{1}{\sqrt{\epsilon_o}} \left[\gamma_p + \left(\frac{\kappa_o^{\text{Th}}}{\kappa_o^{\text{SH}}} \right)^{-1} \gamma_{T2} \right] \quad (9)$$

and is shown by the dotted line in Fig. 51.7. The first and second terms in brackets in Eq. (9) represent the ponderomotive and thermal contributions to the instability, respectively. For given plasma parameters these terms may be evaluated using Eqs. (5)–(7) and provide a convenient guide to the relative importance of the two driving forces. In general the thermal term becomes more important for larger Z and n_o and for smaller λ_o and T_o .

The effect of nonlocal thermal conduction on SBS in inhomogeneous plasmas remains to be studied. Current laser-fusion experiments involve plasmas that are sufficiently inhomogeneous that density and velocity gradients may be expected to determine the threshold, and the incident laser light contains “hot spots” varying widely in intensity. Consequently it is difficult at present to compare theories of SBS (as well as other parametric instabilities) with existing experimental results. Nevertheless, the previous results clearly show that thermal effects must be taken into consideration in modeling SBS in high- Z plasmas, and as experiments approach the long plasma scale lengths and uniform illumination required for reactor-target implosions accurate modeling of this instability will become increasingly important.

In conclusion, we have studied the impact of recent advances in the understanding of thermal transport on the theory of SBS and in particular have developed the theory of a new form of the instability: thermal SBS. This instability bears the same relation to the familiar ponderomotive SBS as thermal filamentation does to ponderomotive filamentation, and we have shown that it is the dominant form of the instability for high- Z , low-temperature, high-density plasmas.

ACKNOWLEDGMENT

This work was supported by the U. S. Department of Energy Office of Inertial Confinement Fusion under Agreement No. DE-FC03-85DP40200 and by the Laser Fusion Feasibility Project at the Laboratory for Laser Energetics, which is sponsored by the New York State Energy Research and Development Authority and the University of Rochester.

REFERENCES

1. P. E. Young *et al.*, Phys. Fluids B **2**, 1907 (1990).
2. K. Tanaka, L. M. Goldman, W. Seka, R. W. Short, and E. A. Williams, Phys. Fluids **27**, 2960 (1984).
3. H. A. Baldis and C. J. Walsh, Phys. Fluids **26**, 3426 (1983).
4. W. L. Kruer, *The Physics of Laser Plasma Interactions* (Addison-Wesley, New York, 1988), Chap. 8.
5. J. F. Drake *et al.*, Phys. Fluids **17**, 778 (1974).
6. W. M. Manheimer and D. G. Colombant, Phys. Fluids **24**, 2319 (1981).
7. L. Spitzer, Jr. and R. Härm, Phys. Rev. **89**, 977 (1953).
8. A. R. Bell, Phys. Fluids **26**, 279 (1983).
9. E. M. Epperlein, Phys. Rev. Lett. **65**, 2145 (1990); E. M. Epperlein and R. W. Short, Phys. Fluids B **3**, 3092 (1991).
10. J. A. Fejer, AGARD Conf. Proc., 13-1 (1973); B. L. Cragin and J. A. Fejer, Radio Sci. **9**, 1071 (1974).
11. W. L. Kruer, *op. cit.*, p. 79.
12. G. W. Hammett and F. W. Perkins, Phys. Rev. Lett. **64**, 3019 (1990).
13. A. J. Schmitt, Phys. Fluids **31**, 3079 (1988).
14. E. F. Gabl *et al.*, Phys. Fluids B **2**, 2437 (1990); D. Ress *et al.*, Phys. Fluids B **2**, 2448 (1990); D. R. Kania *et al.*, Phys. Fluids B **3**, 1496 (1991).
15. C. J. Randall, Phys. Fluids **25**, 2231 (1982).
16. S. I. Braginskii, in *Reviews of Plasma Physics*, edited by Acad. M. A. Leontovich (Consultants Bureau, New York, 1965), Vol. 1, p. 205.

Section 2

ADVANCED TECHNOLOGY DEVELOPMENTS

2.A Anomalous Optical Response of Superconducting Films

The effect of optical (both visible and IR) radiation on the electrical properties of high- T_c superconductors (HTS) has been a subject of active research in the recent years. HTS thin films have been used in a number of devices, including broadband optical detectors,¹ fast-switching devices,² and superconducting quantum interference devices (SQUID's).^{3,4} The HTS films are attractive because they exhibit low reflectivity and a high-absorption coefficient over the visible and near-infrared part of the spectrum.⁵ There have been a series of experiments on infrared detection using HTS thin films, following the development of a nonbolometric infrared detector by Enomoto and Murakami using granular $\text{BaPb}_{0.7}\text{Bi}_{0.3}\text{O}_3$ films.⁶ Fast nonbolometric switching has been observed in optically thin $\text{YBa}_2\text{Cu}_3\text{O}_{7-x}$ (YBCO) films.^{7,8} Subnanosecond switching times have been reported in some cases.⁸

The prime objective of our experiment is to explore the possibility of high-power switching using the optically triggered response in thin epitaxial films. Unlike most other experiments on the photoresponse of HTS thin films, we have used optically thick films (800 nm). The purpose of using thick films is to achieve very high currents. For example, a $1\text{-}\mu\text{m} \times 1\text{-cm}$ switch would carry 100 A at a current density of 10^6 A/cm², and 1 kA at a current density of 10^7 A/cm². In our experiment, a current-carrying HTS film was hit with laser pulses and the resulting electrical signal was measured. We have observed two distinct switching components: a fast nonthermal component (~few nanoseconds) followed by a slow thermal one (~100 ns).

Nonbolometric and Bolometric Components in the Photoresponse of the HTS Switch

The films used in our experiments were deposited on polished 1-cm² MgO substrates using rf magnetron sputtering.⁹ Laser ablation was used to pattern the films into H structures with a central bridge of 2-mm length and width that varied from 100 to 250 μm .¹⁰ This was done by a Nd:YAG laser focused to a 5- μm spot at optimum fluence. The sample was mounted on a gold-coated alumina strip and silver bond pads were evaporated on the sample. A variable dc, constant current source was connected through a 50- Ω coaxial cable to the bond pads on the sample using aluminum wire bonds. The coaxial cables were current-charged transmission lines. The cables were long enough so that no reflections occurred in the time scale of interest. Thus, the influence of the electronic response of the dc current source could be neglected. The other side of the switch was connected to a 50- Ω load across which the voltage was measured. In the superconducting state, the central bridge of the switch acts as a short circuit at the end of the input transmission line and no voltage appears at the load. When the bridge is driven normal, current is diverted to the load and a voltage signal is recorded. The sample was placed inside a cryostat on copper mounts and provided with a temperature sensor. The copper mounts were in contact with the cold finger. A laser beam from a Nd:YAG laser was focused on the bridge using a cylindrical lens to concentrate the energy on the switch. The optical system was chosen to optimize both the intensity and uniformity of illumination at the switch. Energy flux was measured by scanning a razor across the beam. The beam, assumed to be Gaussian, was focused symmetrically on the switch, i.e., the beam axis passed through the center of the switch. The variation of the intensity along the length of the switch was +21% to -34.7% and along the width was +1.5% to -5% about the mean intensities. The fluence was varied, using a wave plate and a polarizer, from 0.5 to 14 mJ/cm². The laser had a pulse width of 170 ps with a repetition rate of 1 kHz. The voltage signal was measured with a 350-MHz oscilloscope and recorded later with a computer-interfaced digitizing oscilloscope. A schematic of the experimental setup is shown in Fig. 51.8.

The observed signal clearly exhibited two switching mechanisms (Fig. 51.9). The slower response, which is believed to be bolometric in nature, was preceded by a faster component having a rise time of the order of a few nanoseconds. The slow thermal component had a time lag compared to the optical trigger, which increased with decreasing laser fluence. The dependence of this time lag of the thermal component, called the response time of the switch, on the laser fluence is shown in Fig. 51.10. For the same laser fluence, this time lag was found to decrease with increasing bias current. A simulation of the bolometric response, described in the next section, exhibited similar dependence of the response time on fluence and bias current. The faster component, which is synchronized with the optical trigger in time, is not of a thermal origin. At present, the origin of this nonbolometric signal component is not clearly understood. It is not associated with the energy redistribution in the film since such a mechanism cannot account for a sharp recovery followed by a secondary thermal rise. The fall time of this signal component is 5 to 6 ns. In the time period that the nonbolometric part of the signal exists, the optical energy is mostly confined to the front surface of the film, suggesting that the signal originates at the surface.

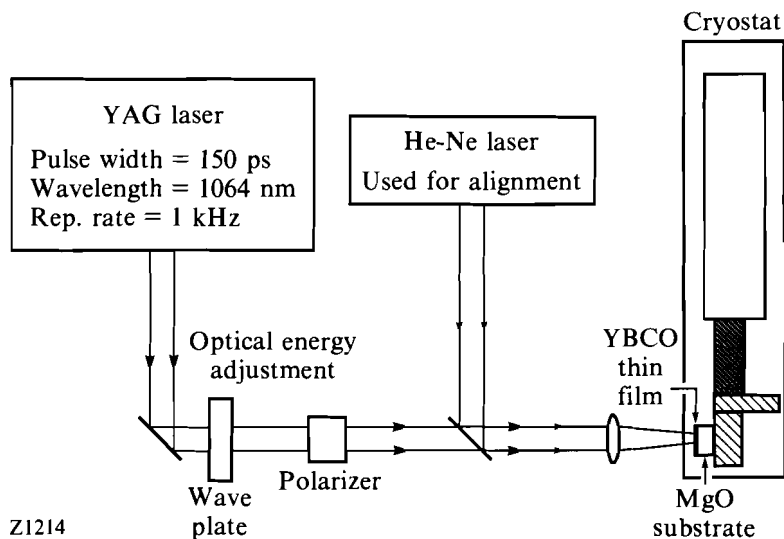


Fig. 51.8
Experimental setup to study the optically triggered switching in HTS thin film.

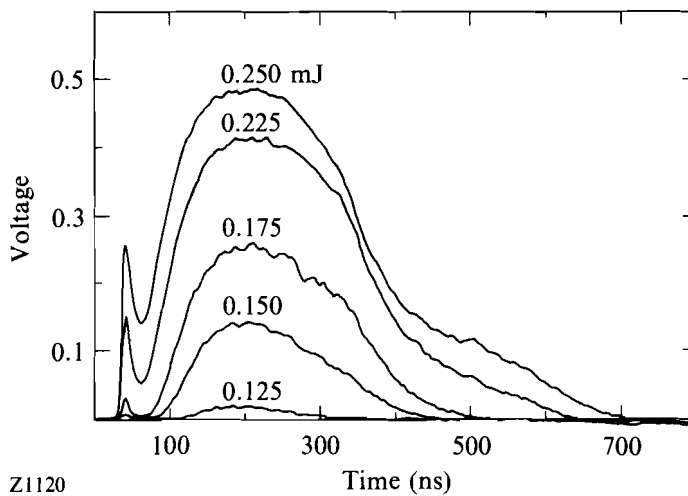


Fig. 51.9
The bolometric and nonbolometric switching components in the photoresponse of YBCO thin film for varying laser fluence. The total optical energy used in each case is shown (about 20% of this energy is absorbed by the switch). The central bridge has dimensions $100 \mu\text{m} \times 2 \text{mm}$. Initial temperature is 70 K and bias current is 30 mA.

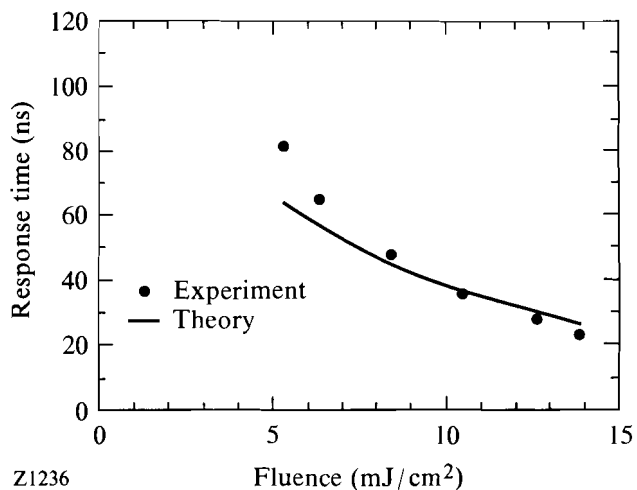


Fig. 51.10
Thermal response time as a function of laser fluence. The theoretical curve is calculated using the peak intensity of the Gaussian energy distribution.

Variation of the initial temperature of the sample permitted the fast signal to be clearly distinguished from the slow one. When the sample is cooled to a temperature just below T_c before hitting it with the laser pulse, the response time of the thermal component is comparable to the width of the fast pulse. This results in a superposed signal that appears to be a single voltage pulse with a sharp initial slope followed by a slow “thermal-like” rise. As the sample is cooled to lower initial temperatures, the thermal pulse starts moving out in time and the overlapping time interval of the two signals becomes smaller. Finally, at low temperatures the two signals are separated in time. Since this temperature is well below T_c ($= 84$ K), usually less than 60 K, we need a high bias current and/or high laser fluence to perform the switching. At low temperatures the critical current is very high, and a significant amount of optical energy is needed to raise the temperature above the critical temperature.

The peak amplitude of the fast signal decreases with diminishing laser intensity. However, its rise time (~ 4 ns), fall time (~ 5 to 6 ns), and response time (time lag relative to the optical trigger) were found to be independent of laser fluence, bias current, and initial temperature. There is a minimum fluence for the fast component to exist for any given temperature and bias current. The thermal component also has a threshold fluence, corresponding to the minimum energy required to raise the temperature of the film above its critical temperature. The threshold fluence for the thermal component is found to be lower than that for the nonthermal component. When the fluence is between these two thresholds, we can observe only the thermal part of the signal.

Modeling and Simulation of the Bolometric Component

We have simulated the thermal response of the laser-irradiated HTS thin-film bridge. The film is divided into 64 slices, each of thickness 125 \AA . The substrate is also divided into 2000-\AA slices. The continuity equation of heat-flow is applied in one dimension (1-D):

$$\partial / \partial x [K(T) \partial T / \partial x] = \rho \partial / \partial t [c(T) T],$$

where K is the thermal conductivity, ρ is the density, and $c(T)$ is the temperature-dependent specific heat.

Thermal conductivity of YBCO film is taken to be $10^{-2} \text{ W cm}^{-1} \text{ K}^{-1}$. The thermal conductivity of crystalline MgO is given by the formula

$$K_{\text{MgO}} = 21.25 - 0.1875 T \text{ W cm}^{-1} \text{ K}^{-1} \quad (60 \text{ K} < T < 100 \text{ K})$$

in the temperature range of interest. Specific heat of MgO is calculated under the T^3 approximation, with Debye temperature (θ_D) of 946 K:

$$c_{\text{MgO}} = \left(12\pi^4 R / 5\right) (T / \theta_D)^3 \text{ JK}^{-1} \text{ mol}^{-1}.$$

The specific heat of YBCO was measured by Ref. 11 and fit with a linear function

$$c_{\text{YBCO}} = 2.83 \times 10^{-3} T - 3.97 \times 10^{-2} \text{ JK}^{-1} \text{ gm}^{-1}.$$

The temperature distribution as a function of distance into the sample is computed by solving the heat equation using the method of finite differences. A time-dependent temperature profile is shown in Fig. 51.11 assuming a uniform illumination of the crossbar with the mean intensity of the Gaussian distribution (13.86 mJ/cm^2) and an initial temperature of 70 K.

This temperature distribution is used to compute the critical current in each slice based on the measured dc characteristics of the film. It is assumed that if at a given instant of time there are some slices with temperature below T_c , they will carry supercurrent unless the current density in the slice exceeds the estimated

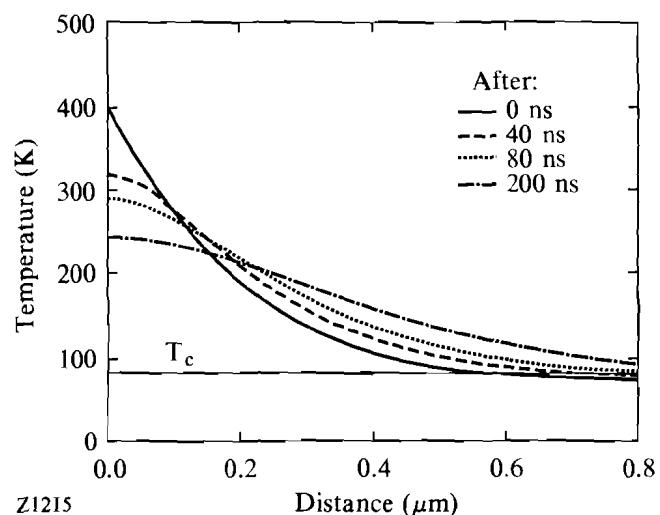


Fig. 51.11
Time variation of the temperature distribution across the thickness of the film.

critical current density. The electrical model is a parallel combination of temperature-dependent linear and nonlinear resistors, one for each slice. If the sum of the critical currents in the slices with $T < T_c$ (I_{sc}) exceeds the applied current (I_0), there is no voltage signal at the output. A slice with temperature above T_c has a normal resistance that varies with temperature. After a period of time, which is called the response time of the switch, I_{sc} becomes less than I_0 and there is a nonzero equivalent resistance in the switch resulting in a voltage signal at the output. This happens because all the slices except a few are above the critical temperature. In this case the output signal is determined by an iterative redistribution of the current between the superconducting and the normal slices. The redistribution is done so that the voltage across all the slices is the same. However, because of the high critical currents of our samples and the small currents we used (<100 mA), this condition ($I_0 > I_{sc}$) was satisfied over a very short period of time. When all slices have $T > T_c$, we have a set of normal resistors in parallel, with resistance varying according to their respective temperatures. In this case, the output voltage can be determined analytically.

Experimentally obtained resistance versus temperature data has been used in this simulation to determine the normal resistance. A set of simulated signals with varying fluence are shown in Fig. 51.12. These correspond to an initial temperature of 70 K and a bias current of 30 mA. The response time of the signal increased as the fluence decreased. The dependence of response time on temperature and the bias current is shown in Fig. 51.13. The response time increases at lower temperatures and lower bias currents.

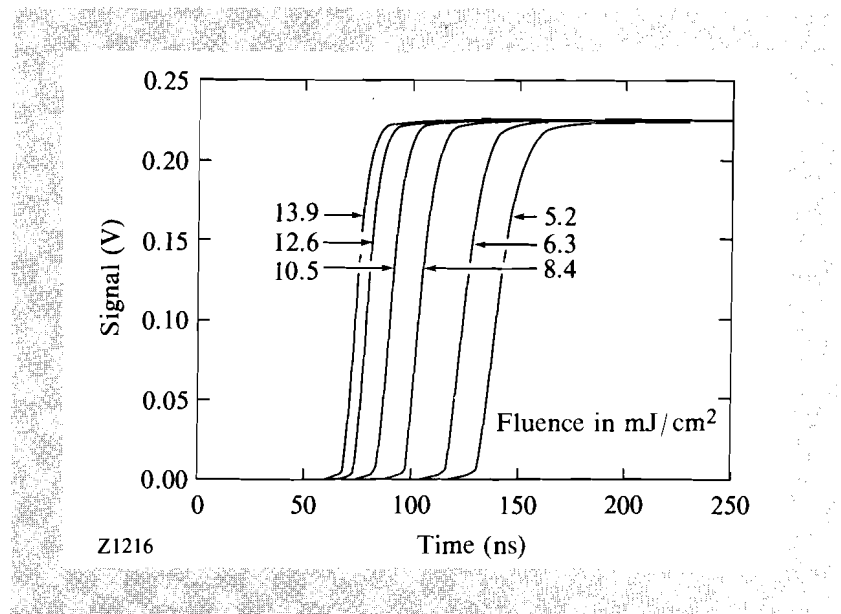


Fig. 51.12
 Simulated signals showing increasing response time for decreasing fluence.

In the simulation, uniform illumination across the switch at the mean intensity was assumed. Without this approximation, the simulation would have been extremely complicated involving a solution of 3-D flow in anisotropic YBCO and a spatially varying resistance function. In the experiment the central portion of the switch receives more energy than the peripheral part and is expected to go

normal while the edges of the switch are still superconducting. Time required for the temperature to exceed the critical temperature will be less than that calculated with the uniform illumination approximation at the center and more at the edges. This can be thought of as a network of normal and superconducting resistors, which in each layer form a mesh. The resistors representing the hot central part of the switch will offer normal resistance while the peripheral ones will be superconducting. Each node in a layer is connected to the corresponding nodes in the neighboring layers. This 3-D network contains time-varying, nonlinear resistors and the analysis becomes complicated. However, a qualitative assessment of the effect of nonuniform illumination on the signal can be made. It will reduce the response time of the switch (by about 10%), since the central part goes normal before the "uniformly illuminated" film. It will also increase the thermal rise time (by about 25%, including the reduction of the response time) because the edge of the illuminated region goes normal after the central region of the film.

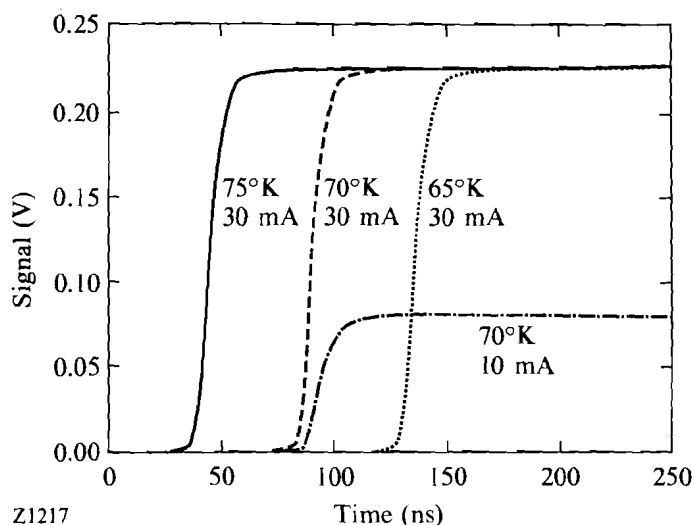


Fig. 51.13
Simulated signals showing that response time increases for lower initial temperatures and lower bias current.

The theoretical curve in Fig. 51.10 is calculated using the peak rather than the mean intensity of the Gaussian distribution. As mentioned above, the peak intensity at the center of the film determines the time at which the sample starts to go normal and, therefore, the response time. The calculated response time is a function of the thermal conductivity of the sample. Values of thermal conductivity higher than the one used in our simulation have been reported.¹¹ A higher value of thermal conductivity would imply faster heat distribution and shorter response time. The value of thermal conductivity corresponding to our experimental response times lies within the range of reported measured values of thermal conductivity of YBCO films.

Conclusion

A fast, nonbolometric switching component has been observed in optically thick (8000-Å) $\text{YBa}_2\text{Cu}_3\text{O}_{7-x}$ films along with a slow bolometric component.

This fast switching (~ 10 ns) occurs at very high current densities ($> 10^6$ A/cm²). The nonbolometric signal had a rise time of ~ 4 ns and a fall time of ~ 5 to 6 ns and its amplitude is a function of the laser fluence.

The bolometric response was simulated by a 1-D heat-propagation model in conjunction with an electrical model describing the electrical response of the film. The results of the simulation were in agreement with the thermal component of the observed signal. The dependence of response time of the simulated signal on initial temperature, bias current, and the laser fluence are consistent with our experimental observations.

ACKNOWLEDGMENT

This work was supported by the National Science Foundation Grant No. DMR-8913524 and by the Laser Fusion Feasibility Project at the Laboratory for Laser Energetics, which is sponsored by the New York State Energy Research and Development Authority and the University of Rochester.

REFERENCES

1. A. Frenkel *et al.*, J. Appl. Phys. **67**, 3054 (1990).
2. W. R. Donaldson, A. M. Kadin, P. H. Ballentine, and R. Sobolewski, Appl. Phys. Lett. **54**, 2470 (1989).
3. J. E. Zimmerman *et al.*, Appl. Phys. Lett. **51**, 617 (1987).
4. R. H. Koch *et al.*, Appl. Phys. Lett. **51**, 200 (1987).
5. M. K. Kelly *et al.*, Appl. Phys. Lett. **53**, 2333 (1988).
6. Y. Enomoto and T. Murakami, J. Appl. Phys. **59**, 3807 (1986).
7. H. S. Kwok *et al.*, Appl. Phys. Lett. **54**, 2473 (1989).
8. M. Johnson, Appl. Phys. Lett. **59**, 1371 (1991).
9. P. H. Ballentine *et al.*, J. Vac. Sci. Technol. A **9**, 1118 (1991).
10. P. H. Ballentine, A. M. Kadin, M. A. Fisher, D. S. Mallory, and W. R. Donaldson, IEEE Trans. Magn. **25**, 950 (1989).
11. C. Uher and A. B. Kaiser, Phys. Rev. B **36**, 5680 (1987).

2.B High-Reflectance Transport-Mirror Development for the OMEGA Upgrade

The transport mirrors that will direct each of the 60 laser beams toward the target chamber are of critical importance to the OMEGA Upgrade. These mirrors, made of complex multilayer coatings, must withstand the full fluence of the OMEGA laser after it has been converted from 1054 nm to 351 nm. This article summarizes the requirements for the mirrors, describes the development procedure and results, proposes a mechanism for the observed damage, and provides a solution for the OMEGA Upgrade configuration.

The high incidence angles required for the transport mirrors have proven to be an important parameter in the study of how the mirrors damage. Initial work established designs, materials, and processes that would meet requirements at normal incidence. However, the mirrors must operate over a wide range of incidence angles and incident polarizations. Designs that work well at normal incidence must be changed for oblique incidence and optimized for a given polarization. Materials differ in their damage characteristics at high incidence angles depending on the type of defect in the film. Substrate preparation and cleaning play a large role in damage of the mirror and can produce large variations in damage thresholds in a series of otherwise identical substrates.

The transport-mirror configuration for the OMEGA Upgrade was changed from a three-mirror to a two-mirror configuration in 1991. This change was made to reduce the effects of stimulated rotational Raman scattering (SRRS) on the beams by reducing the optical path length from the frequency-conversion crystals to the target. One result was an increase in the average angle of incidence on the mirrors (see Fig. 51.14). We will show later that, in general, the laser-damage threshold of the mirror decreases with incidence angle.

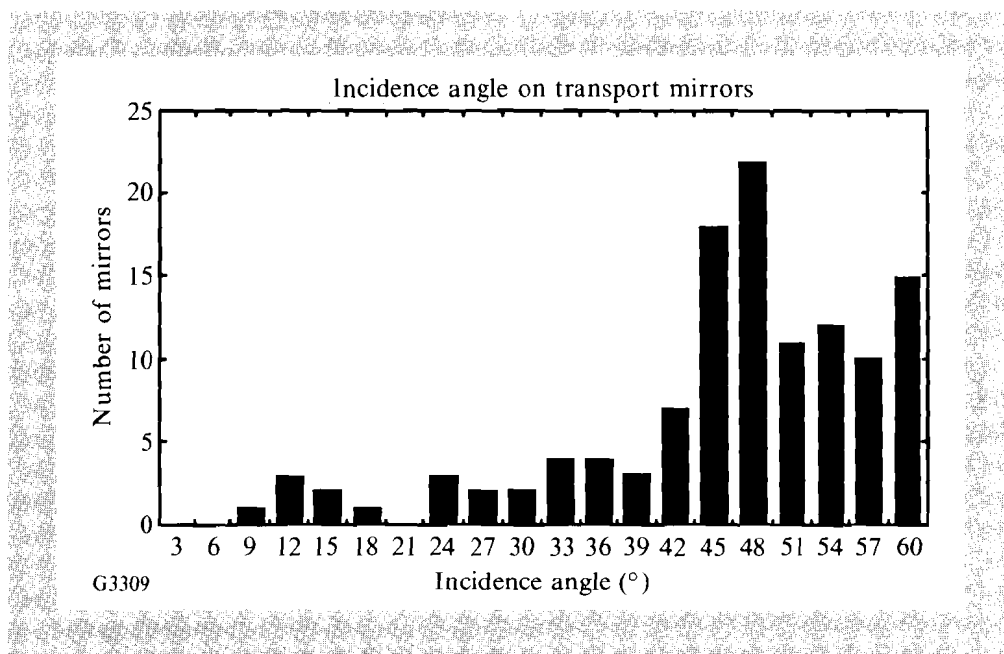


Fig. 51.14

The two-mirror transport scheme for the OMEGA Upgrade yields a high-average-incidence angle. This histogram shows that most mirrors will see an incidence angle between 40° and 60° and more than half of the mirrors will see an incidence angle greater than 47° .

The transport mirrors must reflect 351 nm efficiently without damaging. The reflectance should be higher than 99.5% regardless of incident angle and polarization. The peak fluence of the 351-nm light incident on any optic at this stage in the laser will be 2.8 J/cm^2 for the 0.7-ns main pulse. A second foot pulse will propagate within the annular main pulse with a pulse width five to ten times that of the main pulse. A conservative fourth-root temporal scaling law was used to design fluence loading of the foot pulse under the assumption that the coating would survive the main pulse. The mirrors will also be subjected to unconverted 1054-nm (1ω) and 527-nm (2ω) light. This light also must not damage the coating or the underlying substrate.

Summary of Results for Normal Incidence

Transport mirror coating materials and designs were first evaluated at normal incidence to facilitate both fabrication and testing.¹ The mirrors use two dielectric materials coated in a sequence of layers, which causes constructive interference in the Fresnel reflection from the interfaces. The designs may require more than 30 layers to achieve the required reflectance. Designs are grouped into categories by the dielectric materials used for the layers. A coating design (layer sequence and thickness), the materials, the process used to create the coating, and the substrate are referred to as a high-reflector (HR) system. The results at normal incidence were encouraging and provided several material combinations and process conditions that improved the measured damage threshold beyond the state of the art. In summary the results indicated

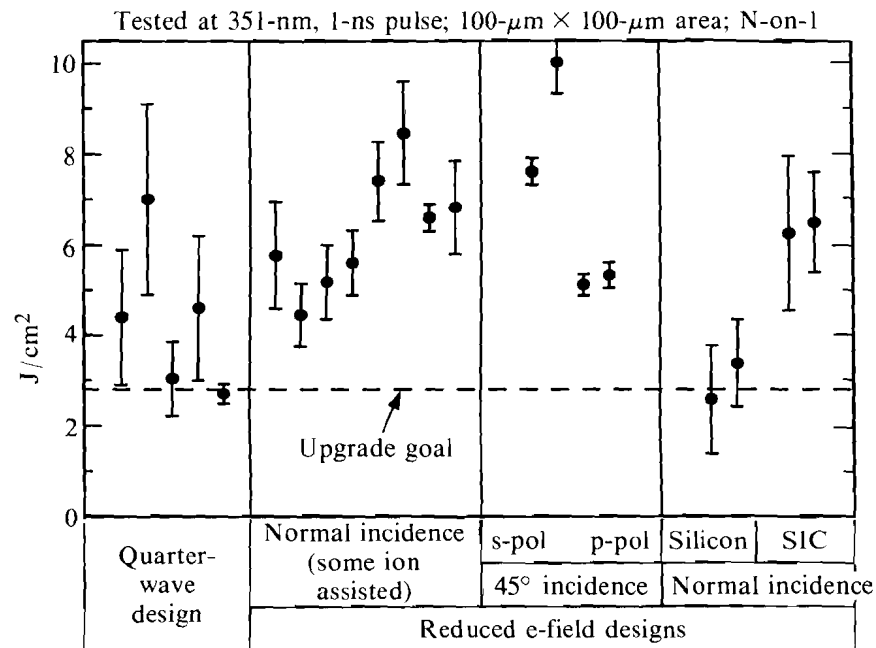
1. Material combinations of $\text{HfO}_2/\text{SiO}_2$, $\text{ZrO}_2/\text{SiO}_2$, and $\text{ZrO}_2/\text{MgF}_2$ had exceeded the Upgrade damage requirement by a significant margin.
2. Designs based on $\text{Sc}_2\text{O}_3/\text{SiO}_2$ had some of the highest thresholds but were deemed too costly to use for all the transport optics.
3. A reduced E -field stack produced the best damage thresholds.
4. An improvement in damage threshold was observed in ion-assisted deposition when using molybdenum grids in a decollimated ion source.

We chose a design based on $\text{HfO}_2/\text{SiO}_2$ for further investigation at high incidence angles because of the higher thresholds of this material pair and the low-UV absorption edge of the hafnia. The damage-threshold data for the $\text{HfO}_2/\text{SiO}_2$ designs at normal incidence exceeded OMEGA Upgrade requirements by a factor of 3 for some samples (Fig. 51.15). These coatings also performed well on silicon-coated silicon carbide substrates, which were considered as a substrate material for the large transport optics. The normal-incidence values exceeded previously published values by a factor of 2 for N -on-1 damage results.

Reduced E -Field Design at Oblique Incidence Angles

High-reflector coatings at normal incidence have shown higher thresholds when designed with suppressed E -field layers at the top of the stack.^{2,3} Absorption at a film defect site will be proportional to the electric-field intensity. Known areas of high absorption, such as interfaces between materials, can be intentionally located at regions of lower electric-field intensity. Usually this means that other low-absorption areas will see a higher electric-field intensity. This trade-off has been used to increase thresholds by a factor of 1.6 for coatings of $\text{Sc}_2\text{O}_3/\text{SiO}_2$.⁴ We have found a similar improvement for coatings at normal incidence. Figure 51.16 illustrates the reason for the improvements. In each frame the time-averaged square of the electric field is plotted within a multilayer (the incident wave arrives from the right). The peak of the standing wave on the right side in the incident media is cut off in these plots, but will be very close to 4 in a high reflector. The first frame [Fig. 51.16(a)] shows the field plotted in the simplest case: a quarter-wave optical thickness stack at normal incidence. The nodes and antinodes of the electric-field intensity are located at the interfaces between the high- and low-index materials. The peak antinodes of the standing wave drop rapidly as the field penetrates the multilayer (a line has been fitted to these

points). The high intensities at the interface are suspect in initiating damage in a high reflector. In the following frame [Fig. 51.16(b)], the thickness of the layers has been modified in the design so that the standing-wave intensity is the same for the top three interfaces of the multilayer (all layers are shown as equal thicknesses in this figure for clarity). The secondary effect is to increase the standing-wave intensity within the homogeneous low-index layer, but, since this layer is composed of a low-absorption material (silica), the overall effect is to increase the damage resistance of the coating. The increase in damage threshold has been documented at normal incidence for mirrors at 351 nm.



G3062

Fig. 51.15
HfO₂/SiO₂ designs have met Upgrade requirements at normal incidence. At a 45° incidence angle differences in the threshold for the two polarizations emerge. The coating thresholds also drop when deposition is on substrates other than glass.

At oblique incidence the E -field must be evaluated separately for s- and p-polarized light. An example of the E -field plot for a 45° unsuppressed reflector is shown in Fig. 51.16(c). Here again the nodes and antinodes are at the interfaces, but now there are two separate plots for the two polarizations. The E -field intensity for the p-polarized light is also discontinuous at the antinodes. If a suppressed E -field coating is designed for normal incidence, it can be “tuned” to operate at an oblique incidence angle by increasing the thickness of all the layers proportionately. The plot for the E -field intensity will then appear as in Fig. 51.16(d). Here neither the s- nor the p-polarized intensity at the interfaces is level, but instead the s-polarized component decreases and the p-polarized component increases in the first three layers of the coating (this design only modified the top two antinodal interfaces). A level E -field design can be attained for one, but not both, polarizations by substituting the appropriate effective index in the original equations supplied by Apfel.³ Instead of using the index n_i for a given material, substitute

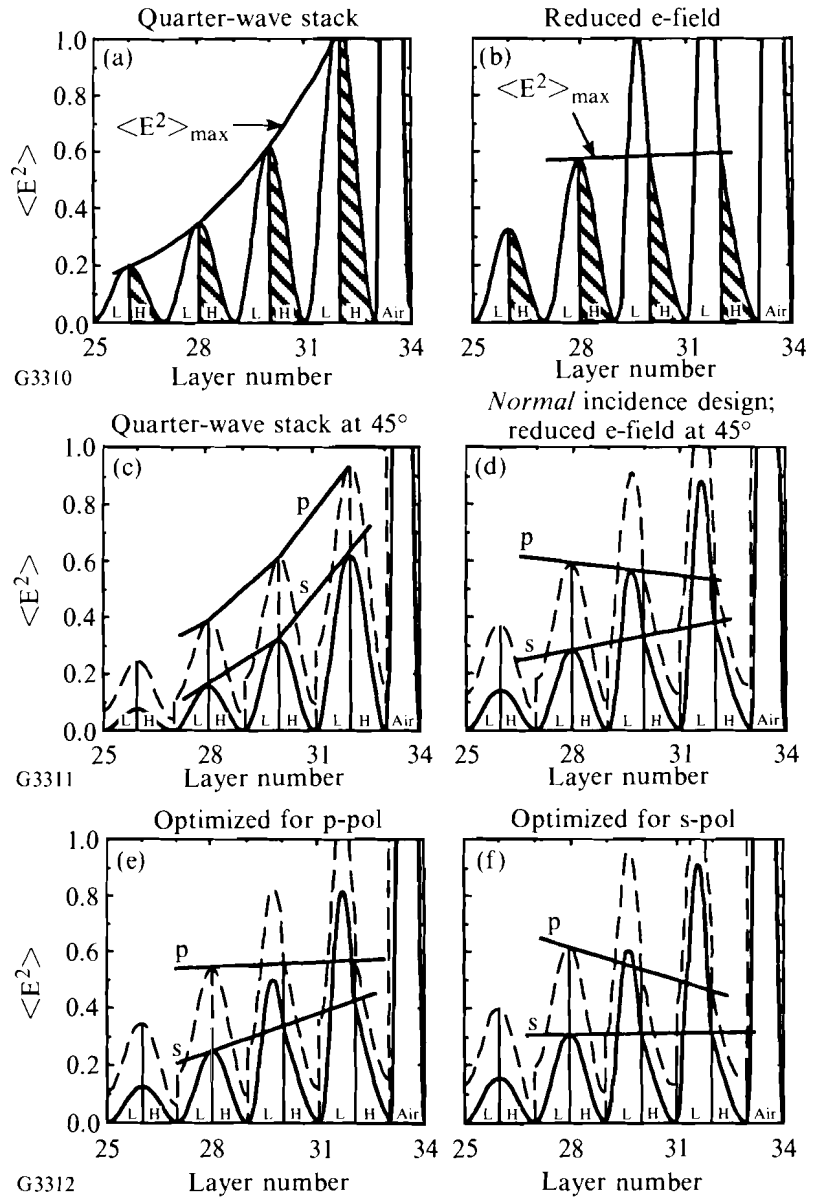


Fig. 51.16

The electric-field standing wave in a thin-film stack can be altered to improve the damage threshold. Each frame shows a plot of the top layers in a stack with the time-averaged square of the electric-field magnitude superimposed over the layers. The H and the L represent high- and low-refractive index layers. A line connects the peak magnitude at the interfaces where high absorption levels could lead to damage. The different frames show the E -field for different designs, incidence angles, and polarization: (a) normal incidence, unaltered quarter-wave-thickness stack; (b) normal incidence, reduced E -field for top six layers; (c) quarter-wave-thickness stack, s- and p-polarization; (d) 45° incidence, reduced E -field for top six layers using normal incidence design; (e) 45° incidence, reduced E -field for top six layers using design optimized for p-polarization; and (f) 45° incidence, reduced E -field for top six layers using design optimized for s-polarization.

$${}^s\eta_i = n_i \cos\theta_i \text{ for the s-polarized case,}$$

$${}^p\eta_i = n_i/\cos\theta_i \text{ for the p-polarized case.}$$

All indices should be converted to the effective index including the incident and substrate. The result is a design optimized for s-polarized light [Fig. 51.16(e)] or a design optimized for p-polarized light [Fig. 51.16(f)]. In the first case, the design for a level E -field intensity in s-polarization produces an E -field intensity increasing with depth for p-polarization. Since thresholds for s-polarization are generally higher than p-polarized threshold, we do not expect this design to be of great utility. The design optimized for p-polarization provides suppressed E -fields at the interfaces in p-polarized light and improves, but does not optimize the E -field intensity for s-polarized light. While an attempt was made to verify these designs experimentally, the results have been obscured by sample variation, as will be discussed in the next section.

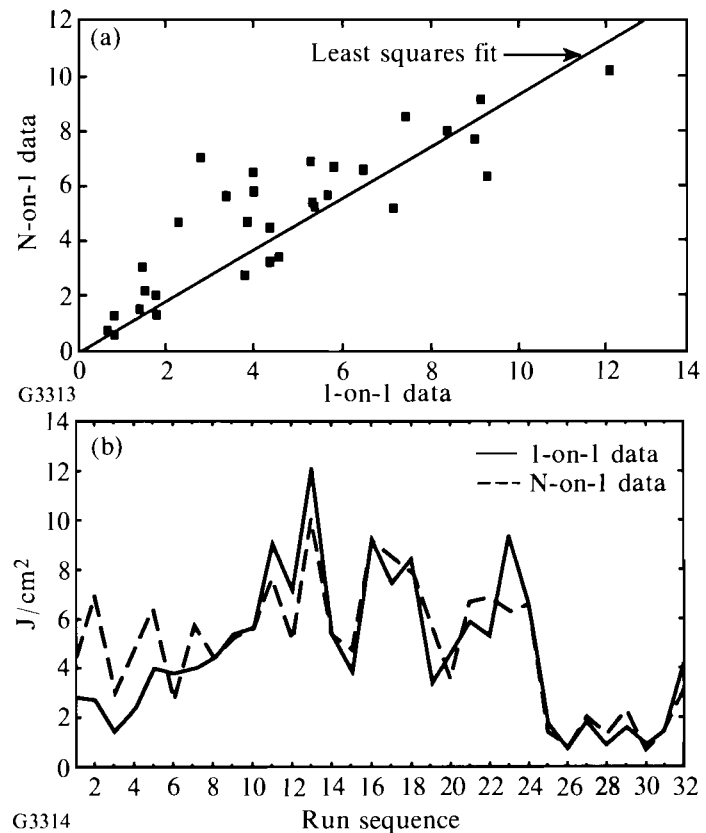
Damage Testing Process for the Oblique Angle Tests

All reflector coatings are tested in the LLE damage-test facility with 351-nm, 0.7-ns, FWHM pulses. Either 1-on-1 or N -on-1 (sometimes both) testing is performed on the samples. In 1-on-1 testing, a new site is chosen for each laser shot. A minimum of ten sites are usually examined. The 1-on-1 damage threshold is defined as the average of the highest nondamaging fluence and the lowest damaging fluence seen in all sites. In N -on-1 testing, one site is subjected to successive laser pulses, each one increasing in fluence above the previous pulse until damage is observed. Three to ten sites are tested in this manner, and the fluences at which damage occurs are averaged to give the N -on-1 damage threshold. N -on-1 testing is more typical of the operation of a large laser facility, demonstrating a hardening effect in the tested surface.⁴ Damage is assumed to have occurred whenever a new scatter site appears within a $100 \times 100 \mu\text{m}$ area observed under dark-field incandescent illumination.

For a restricted coating system, 1-on-1 testing may be used exclusively for comparing and predicting laser damage. In previous years, all samples were subjected to 1-on-1 and N -on-1 testing. While 1-on-1 measurements are faster, N -on-1 measurements more accurately reproduce the behavior of coatings in a multiple-shot laser. Unexpected differences in the two measurements have previously supported taking both measurements when examining widely diverse coatings and optical devices. However, when a single-coating system, the $\text{HfO}_2/\text{SiO}_2$, 351-nm-high reflector was examined, a strong correlation between the 1-on-1 and N -on-1 data was observed. The data from one year of N -on-1 and 1-on-1 tests for the hafnia coating are plotted parametrically in Fig. 51.17(a). A linear fit to the data shown in the figure returns a slope nearing unity. The same data are also plotted against run sequence in Fig. 51.17(b). These data imply that (1) when testing a thin-film multilayer made with tight process controls, the 1-on-1 data are a reasonably good predictor for the N -on-1 data, and (2) there is little indication that a “conditioning” effect occurs with many of these coatings. The absence of conditioning in 351-nm reflectors has also been noticed by investigators at LLNL when examining films using ramped pulses (R -on-1) testing.⁴ Subsequent testing to examine effects of angular sensitivity on the hafnia coatings primarily used 1-on-1 testing to increase throughput.

Fig. 51.17

For a given coating system (same materials, same design) the 1-on-1 damage threshold can accurately predict the N -on-1. In Fig. 51.17(a) the 1-on-1 threshold is plotted against the N -on-1 threshold for a series of hafnia/silica mirrors. A linear fit to this plot has a slope near unity indicating that these films show almost no hardening. In Fig. 51.17(b) a plot of the same data against run sequence shows how closely the two measurements can track each other, thereby reducing the need to make time-consuming N -on-1 measurements.



Previous damage tests indicated that detected thresholds might vary with the time of day, location of test site on the sample, and the environmental condition of the lab. These variations might be a result of equipment warm-up, reliability of the algorithm for determining the peak fluence, sample cleanliness, or changes within the coating itself (aging effects). To test these factors, we used an experimental design approach⁵ that allowed several experimental factors to be tested in one experiment. Five identical substrates were prepared and coated simultaneously with a hafnia reflector tuned for a 60° angle of incidence. A 1-on-1 damage test at 351 nm was performed on each of the four quadrants of the substrate. The four quadrants were tested randomly on different days and at different times during the day. The results [Fig. 51.18(a)] verified that the testing process was giving repeatable results, and most of the measurements showed little variation in either time of day tested, the test date, temperature, lab humidity, or quadrant on the sample. The results did show an unexpected variation among the different samples. These results were surprising, especially in view of the extra effort that went into handling of the substrates. Each substrate was from the same vendor, was cleaned in the same process, and was held in a stainless steel mounting fixture placed in a nitrogen-purged atmosphere after the coating process. Despite these controls on the process, the sample variation dominated the results. The experiment was repeated with a less extensive test sequence to ensure that the results were not caused by an isolated poor coating

run. The second test [shown in Fig. 51.18(b)] shows an even lower threshold with less variation. Both tests indicate that some part of the process introduces variability in the samples, which greatly reduced possible thresholds. The variation of samples coated in the same run indicates that either the deposition process produces a coating that has variable properties across the substrate rack, or the substrate preparation processes are not consistent. The optical uniformity of the substrates is very tightly held by using an elaborate planetary rotation in the system. No measurable quality of the films correlates with the differences in the damage thresholds. These two experiments gave strong evidence that the individual substrates must vary in either the polishing method or the cleaning techniques prior to coating.

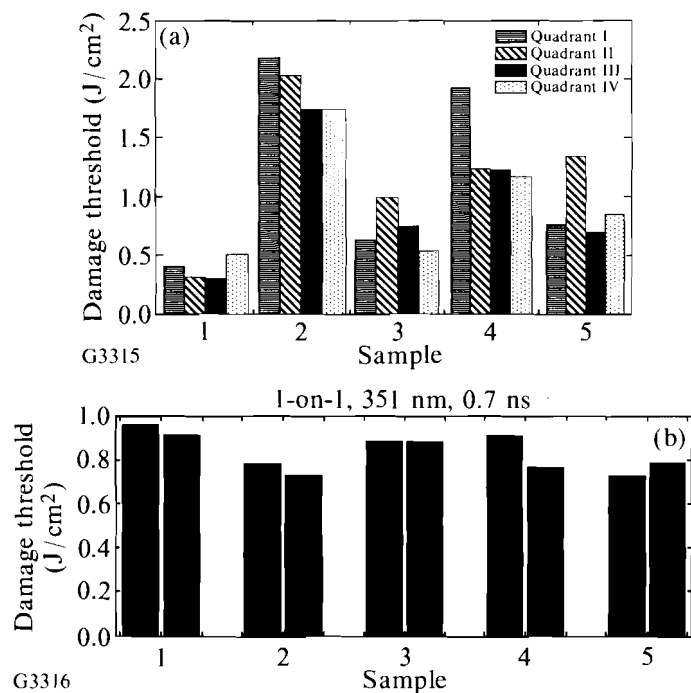


Fig. 51.18

Two experiments were performed to verify repeatability of the testing processes. Samples from the same coating run were tested at different times, days, and sample locations. In Fig. 51.18(a) the samples were tested in four different quadrants, each giving consistent results within each sample and high variation from sample to sample. The results in Fig. 51.18(b) verified the first experiment but with less sample-to-sample variation. Both experiments gave early indications that variations might be caused by substrate preparation.

HR Coatings at High Incidence Angles

The damage threshold drops for most HR coatings when they are examined at incidence angles higher than 40° . A compilation of damage tests at a range of incidence angles for one coating (hafnia/silica) is given in Fig. 51.19. Each of the coatings was tuned to operate at the specified test incidence angle. The decrease in damage threshold tends to be greatest for p-polarized light incident on the substrate. The damage threshold can increase at high incidence angles for s-polarized light in a few isolated tests. The measured damage threshold was found to be sensitive to the damage-test, laser-incidence direction in a number of tested coatings. This observation may appear counter-intuitive since the actual flux density in the plane of the mirror decreases with a higher angle of incidence. It is important to note that the reported damaging fluence at any given angle of

incidence is always defined as the fluence measured in a plane perpendicular to the propagation direction (this is the same plane in which the electric and magnetic vectors lie in the incident media). Actual fluence in the incidence media at the substrate plane may be found by multiplying by $\cos\theta$. It would be expected that this cosine factor would allow the threshold to increase as the incidence angle increases. However, this is not the case with the tested coatings that ranged from 0° to 63° in incidence angles. One reason for this phenomenon is that the Fresnel reflection at all the interfaces drops for p-polarized light and the high-magnitude electric fields penetrate further into the films at the higher angles.

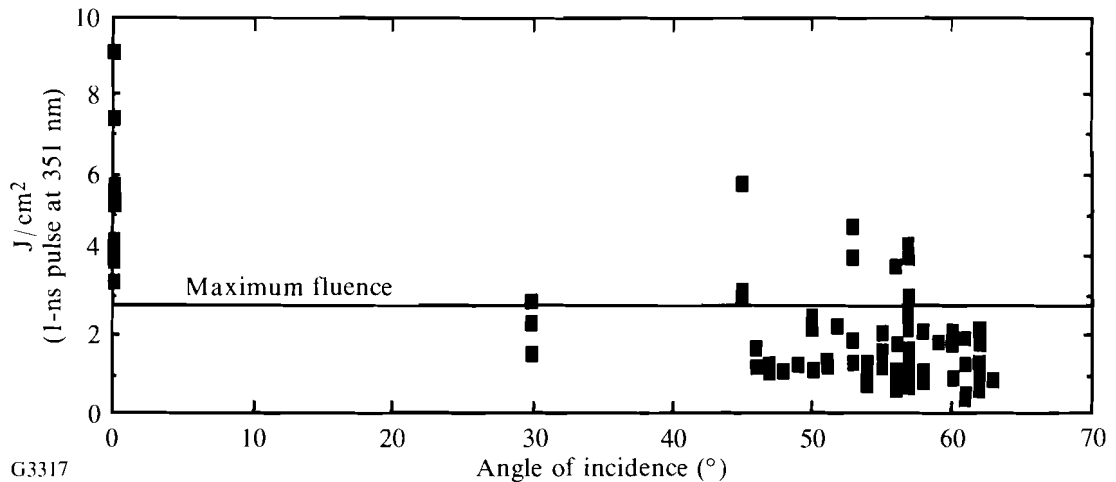


Fig. 51.19

The damage thresholds decrease for the hafnia/silica high reflectors at higher angles of incidence. The thresholds shown are from a series of coatings optimized in reflectance for the test angle and tested with p-polarized light.

A dependence on the test-beam incidence angle was found for some of the HR-coating systems in the study. As the incidence angle increases, the reflectance band for p-polarized light decreases in width. This limits the range in angle over which the mirror will operate. For example, the angular range of high reflectance for a normal-incidence HR will be 0° – 30° while the range for a 55° HR will only be 50° – 59° . If the damage test beam is scanned through this angular range for a given coating, the threshold will drop off precipitously on some samples. An example is given in Table 51.I. This hafnia/silica sample dropped by more than a factor of 2 in damage threshold when the damage-test beam incidence was 3° from the peak reflectance. The corresponding reflectance values varied only a small amount over this range. This effect was seen only in some of the samples.

The variation of damage threshold in the hafnia/silica coatings at oblique angles suggested that further study would determine the main factors for the variation. Some of these coatings had thresholds as high as 5.7 and 4.2 J/cm² for incidence angles of 45° and 53° , respectively. Adequate thresholds were attainable with this material pair but not repeatable. Using experimental design techniques, an experiment was conceived that tested nine different factors in eight separate coating runs using 32 samples (Design of Experiments 2 - DOX2). The factors were all assigned two possible states, as described in Table 51.II.

Table 51.I: Some (but not all) high-reflector coatings experience a sharp drop in damage threshold when tested over a range in angles. The reflectance remains at a high value over the same range.

Angle of Damage Test	1-on-1 Threshold @ 351 nm, 1 ns J/cm ²	Reflectance
51°	1.48±0.08	0.995
53°	4.70±0.02	0.996
55°	4.37±0.30	0.995
57°	1.75±0.01	0.994

G3341

Table 51.II: Factors and values in the DOX2 experiment.

Factor	State 1	State 2
Spatter from <i>e</i> -beam	Low	High
Hafnia starting material	Fully oxidized	Reduced (grey)
Coater operator	Staff A	Staff B
Ion pre-clean	Yes	No
Oxygen	Normal	Ionized
Substrate temperature	150°C	200°C
Reduced <i>E</i> -field design	No	Yes
Substrate	BK7 - Vendor A	Pyrex - Vendor B
Substrate cleaning	Staff C	Staff D

G3342

The surprising result from this experiment is that none of the factors were important predictors of damage threshold, even though the factors had been picked because they had previously exhibited an effect in other experiments. The average threshold of the samples in DOX2 is 1.43 J/cm² with a standard deviation of 0.52 J/cm². As with the DOX1, the prevailing variation was caused by noise apparently from sample to sample. The only factor that might have an effect is the use of reduced *E*-field, but even this factor is of questionable statistical significance. In the best case, using the same process as DOX2, 95% of the future thresholds are expected to be in the range 1.7±0.9 J/cm² in the best case. After DOX2 results, it was clear that some factor in the preparation of the samples before coating was causing significant variation in the samples.

The effects from a wealth of processing steps for the substrate could be eliminated by cleanly cleaving the glass. A cleaved surface will also not require cleaning prior to coating. Typically, polished substrates are scrubbed with a fine polishing compound and a detergent, washed and rinsed in high-purity water, and air dried in a class-10 environment prior to placement in the coating chamber. However, past researchers have had difficulty obtaining a cleave without also creating residue from the fracturing process.⁶ We found that an excellent cleave may be obtained by use of a microtome knife cutter.⁷ Using this device, we were able to produce featureless cleaves in float glass and BK7 glass (Pyrex and fused silica did not cleave well). The cleave showed no particles when observed under dark-field microscopy and was comparable to the cleanest damage-test substrates we have seen.

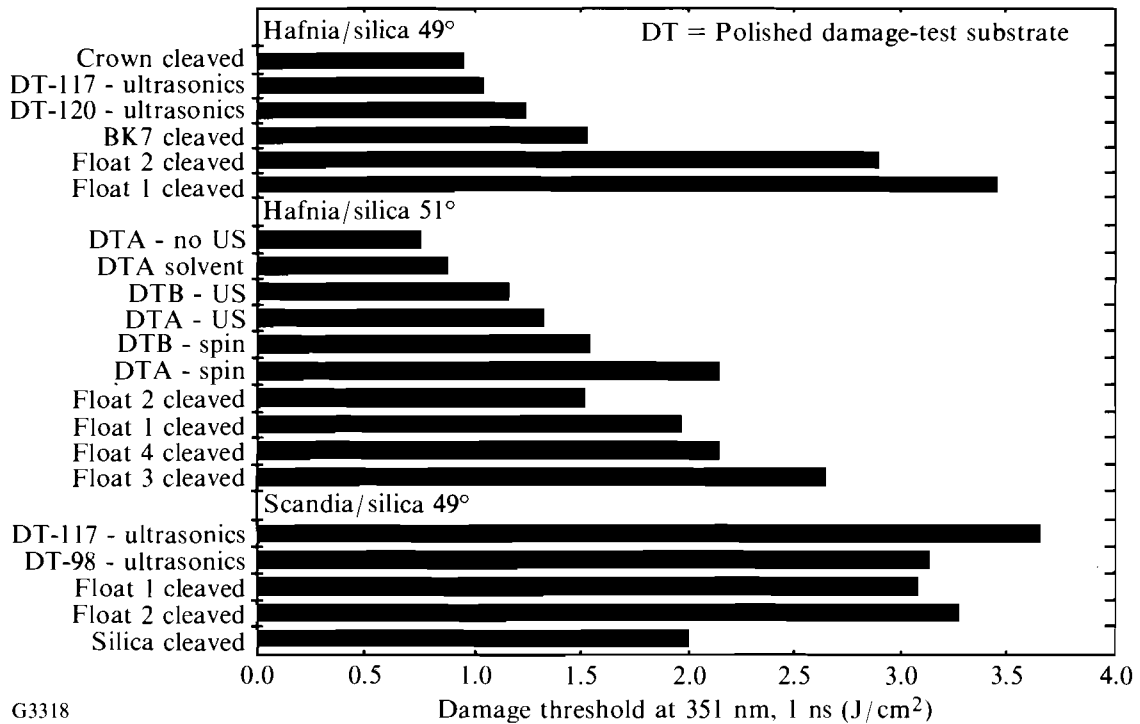
A set of test runs were made with both cleaved and polished glass in the substrate holders. The first run, a hafnia/silica HR at 48°, tested with threshold significantly higher on cleaved float glass than the polished damage test substrates (Fig. 51.20). Two other types of glass, BK7 and a crown glass, showed thresholds as low as the polished pieces. In a second test, seen in the bottom half of Fig. 51.20, various methods of cleaning the damage-test substrate were compared to cleaved samples. These tests indicate that the ultrasonic wash part of the cleaning cycle may be related to the low-damage threshold. Parts cleaned without ultrasonics and dried by spinning had thresholds comparable to or better than the cleaved float. These results fully support the previous results that found sample-to-sample variation was dominant. A discussion of how substrate contamination might affect damage threshold is included.

Scandium Oxide

The scandium oxide/silicon dioxide material pair has provided high thresholds at normal incidence in both LLNL⁴ and LLE² studies. We examined the characteristics of several oblique incidence coatings made from scandia and compared them to normal incidence coatings (Fig. 51.21). While all these coatings meet the damage requirements, they do show the drop in threshold as the incidence angle increases (p-polarization). The few results here do not have as strong a correlation between 1-on-1 and *N*-on-1 threshold as the hafnia results; but the *N*-on-1 results are always higher than the 1-on-1 results, which is caused by the well-known “conditioning” effect seen for some coatings.

The sensitivity of threshold to test incidence angle was exhibited by a 57° scandia reflector. A coating tested at 55°, 57°, and 59° gave 1-on-1 thresholds of 1.7, 3.2, and 2.2, respectively. Once again the acceptable angular range is much lower than would be expected from reflectivity curves. The scandia/silica coatings are less sensitive to substrate contamination than the hafnia coatings. A coating made simultaneously on cleaved and polished substrates produced very small differences in damage threshold (Fig. 51.20, bottom).

Scandia’s promising results make it a good candidate for coating transport optics, although a major drawback is the cost of the material. The 12 kg required to coat all the transport optics would be a major, and possibly prohibitive, cost for the OMEGA Upgrade. Most of the spent material in the deposition chamber could be reprocessed to limit material cost in these runs, but a supplier would



G3318

Fig. 51.20

A cleaved glass surface provides an excellent control surface to study the effects of substrate preparation. Several type of surfaces were coated simultaneously and the damage tested at the stated incidence angle with p-polarized light. The damage test substrates (DT, A and B designate vendors) were cleaned in an aqueous process with either drying by spinning or with ultrasonics and drying in air. The soda-lime float glass produced the cleanest cleaves and also gave the highest thresholds for the hafnia/silica reflectors. The thresholds of scandia/silica reflectors were less dependent on the substrate condition.

have to be found who could hot press the material into a form well suited for e-beam deposition.

Defects and Damage at Oblique Incidence

The predominant finding in this study is the decrease in damage threshold with increasing incidence angle despite the $1/\cos\theta$ geometric fluence dilution. The variation in threshold within samples suggests a defect-driven damage mechanism. Boyer *et al.*⁸ state that the damage threshold fluence for a series of mirrors at 248 nm also decreased for p-polarization. They proposed a model of cylindrical defects oriented normal to the surface in the film, which would expose a greater surface area to the beam at high incidence angles. This proposal, while plausible, does not provide an explanation for the steep drop in thresholds for p-polarized light we have seen in all our samples, nor does it give an explanation for the sensitivity to angular and substrate-contamination effects.⁹ The authors point out that absorption in the multilayers may explain the simple fluence dependence at 248 nm.

The films produced for this study have two predominant types of defects, nodular¹⁰ and spatter. The nodular defects usually grow around a small seed ($\sim 0.5 \mu\text{m}$) and in a conical shape, as schematically shown in Fig. 51.22(a). The seeds may be left from a polishing or cleaning process, and they occasionally occur within the growing film itself. The nodule achieves a domed appearance at the top layers with a dimension dependent on total film thickness. The domed

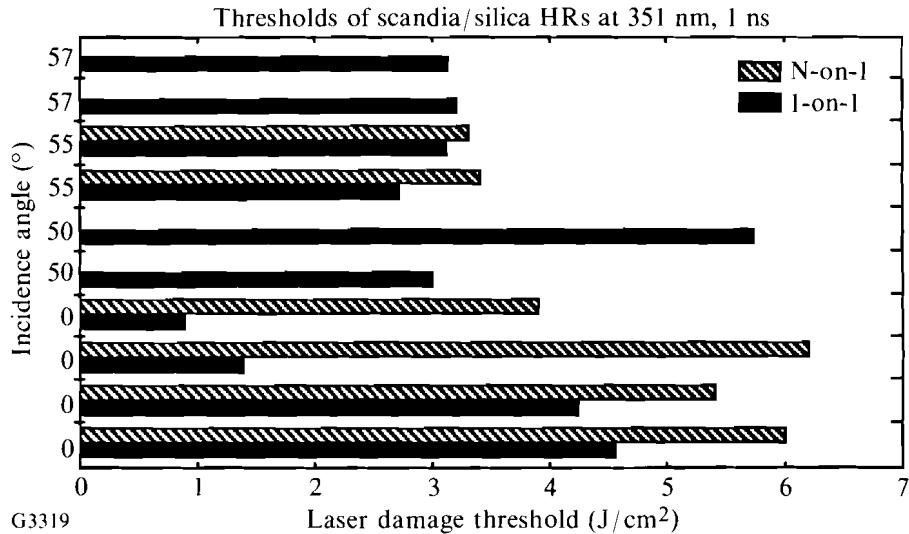


Fig. 51.21

Scandia/silica reflectors maintained high damage thresholds even when tested at high incidence angles with p-polarized light. The scandia reflectors also demonstrated a conditioning effect as shown by the increase of N-on-1 from 1-on-1 test results.

top consists of the top layers of the multilayer, which can adequately reflect away any radiation that might otherwise be absorbed by the defect below. Spatter consists of ejected matter from the evaporant melt in the *e*-beam source. Some materials, such as hafnia, tend to reduce to a sub-oxide or metal-rich melt, explosively throwing up copious numbers of particles from the melt. The particles are composed of the sub-oxide melt and range in size from 1 to 10 μm when they arrive at the substrate. The particles are often cylindrical in overall shape and orient with the axis perpendicular to the surface, as seen schematically in Fig. 51.22(b). Figure 51.23(a) shows a scanning electron micrograph of one of these features in a hafnia/ silica film. After forming on the surface, the particle may itself be coated with the remaining multilayer HR coating, as shown in Fig. 51.22(b). Scandia films have very few spatter defects (1 to 2/mm²), while hafnia films show a high density (80 to 150/mm²) of spatter. Both films have an approximate density of nodules of 50/mm².

The spatter defects appear to be responsible for the decrease in threshold of the hafnia film. Figure 51.23(a) shows a SEM view of a spatter on a film after coating. The density of these defects seen in the SEM match the density of the defects seen in dark-field optical microscopy. A different substrate from the same run was exposed to a high-fluence, large-aperture 351-nm beam at an incidence angle of 51°. A scan with the SEM showed only remnant cavities where the spatter had been [Fig. 51.23(b)]. The spatter is protected at normal incidence from the light by a bit of multilayer coating, which covers the top of the defect. At oblique incidence, the light reaches the side of the spatter particle itself where the material is likely to have the same high-absorption characteristics as the melt. (The film itself is evaporated reactively with oxygen to promote reoxidation at the substrate surface.) Thus, the apparent threshold for hafnia may be low; but once the defects have been ablated, the thresholds may be quite high. At present, an investigation is being conducted with a large-aperture beam to test this premise.

Fig. 51.22

The damage mechanism for hafnia films is defect dominated. Two types of defects appear in these films. Figure 51.22(a) shows the nodule defect, which is a growth defect occurring around a submicron seed on the substrate. The domed area at the top of such a defect may produce a range of incidence angles high enough to admit light into the lower regions of the stack. The angles θ_i , θ_f , and θ_n have the values 49° , 75° , and 24° , respectively, in this model. These reflectances of a high-reflector design at these angles are also marked in Fig. 51.24. Figure 51.22(b) shows a rendition of spatter defects from ejected material in the melt. These spatter defects are highly absorbing and will eject when illuminated in oblique incidence. At normal incidence the defect will be protected by a sheath of the multilayer mirror coating.

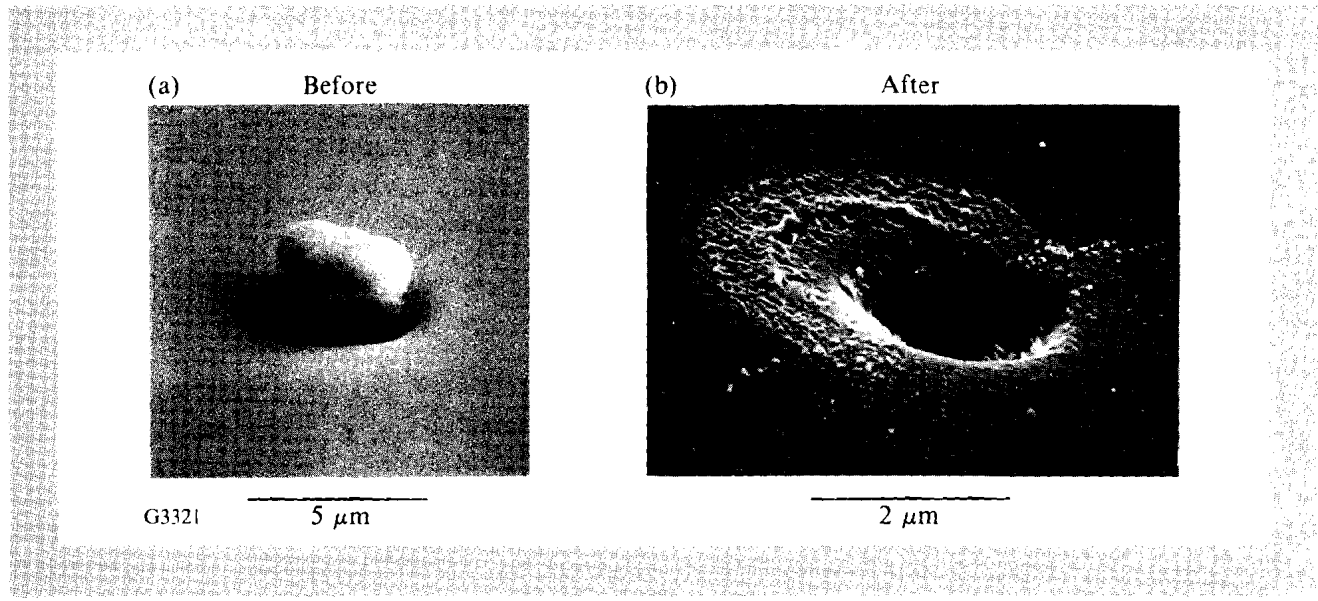
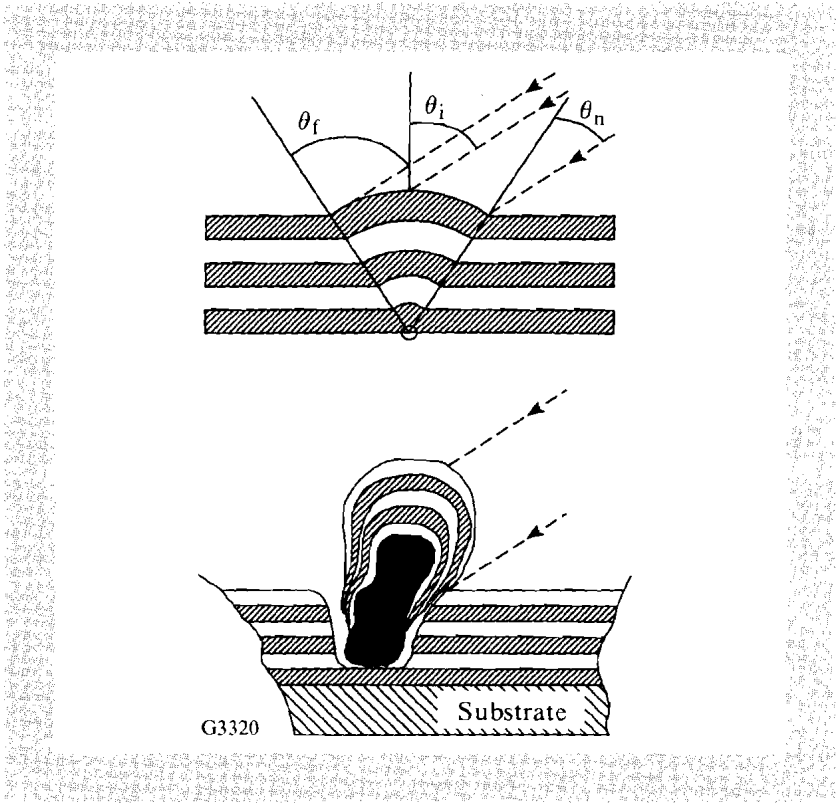


Fig. 51.23

The scanning electron micrographs document the change occurring in a spatter site in a hafnia/silica mirror before and after large-beam testing. An optic examined before exposure shows multiple spatter defects similar to those in Fig. 51.23(a). In Fig. 51.23(b), the defects are seen after exposure to a 351-nm, 1-ns pulse at $>3 \text{ J/cm}^2$. They appear to leave behind a crater after being ejected from the surface. The increased scatter from the crater will be interpreted as damage. The spatter and nodule defects can be distinguished from one another by the size and defect density in the film.

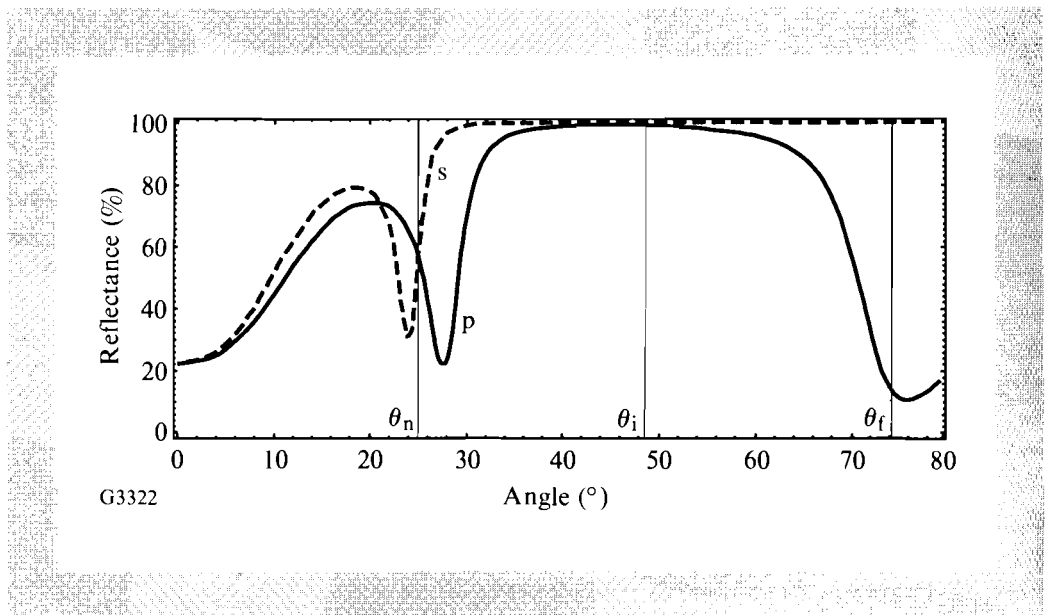
The damage in some of the hafnia and scandia films may be dominated by nodular defect. At oblique incidence, the incident angle at the edge of the defect will be different than the incident angle at the center of the dome [Fig. 51.22(a)]. At near-normal incidence, the change in angle from center to edge will have little effect since the reflection band has a wide bandwidth in θ -space. Two effects predominate at high θ : (1) Since the phase-thickness β of a thin film goes as

$$\beta = \frac{2\pi nd \cos \theta}{\lambda},$$

the phase thickness changes more rapidly at high angle, and (2) as θ increases, the reflection bandwidth decreases for p-polarization. At high incidence angles, the change in θ_n may allow light to pass through to the defect in p-polarization, thereby causing absorption and damage. Since the bandwidth for s-polarized light is much greater, the defect would see less light and be protected from damaging (Fig. 51.24). This effect may be responsible for the incidence-angle sensitivity seen in some of the coatings.

Much of the evidence presented in this article supports this defect-dominated damage model. Hafnia and scandia both have absorption edges near 220 nm and thresholds exceeding 5 J/cm^2 at normal incidence, but hafnia thresholds drop faster at oblique angles. Hafnia produces copious amounts of spatter during *e*-beam deposition. All samples analyzed have shown a distribution of defects in the coating, which probably originated from this spatter. We have found it is possible to reduce the number of defect sites but not to eliminate them entirely. Despite these defects, the hafnia coating may operate well enough if the damage surrounding the ejected spatter site does not propagate. Scandia, which has reasonable damage performance at oblique angles, has a very low spatter rate during deposition and only forms nodules around defects existing on the substrate.

Fig. 51.24
The limited angular acceptance of the dielectric, high-reflector coating may allow damaging radiation to reach defects under a nodule. This plot shows the calculated reflectance for s- and p-polarization for a hafnia/silica high reflector as a function of incident angle. The design peaks in reflectance at 50° for 351-nm light. The angles θ_i , θ_f , and θ_n refer to the incident angles across a nodule in Fig. 51.22(a).



Transport Optic Design for the OMEGA Upgrade

A scandia/silica reflector design would be the best choice for the OMEGA Upgrade transport mirrors, but the cost of materials for all the test and product runs may be prohibitive. Alternatively, the hafnia/silica high reflector should have acceptable performance for low-incidence-angle optics and for high-incidence-angle optics with the electric vector predominantly s-polarized on the optic. Figure 51.25 is a plot of all 120 transport mirrors with incidence angle at the horizontal axis and portion of energy in the s-direction on the vertical axis. The shaded portion represents an area in which all the coatings will be the scandia coating. The input polarization to the target-mirror system can be $\pm 35^\circ$ from the horizontal axis and will be determined by minimizing the number of scandia-based reflectors.

Continued effort will be made to find the criteria for switching to scandia designs. The causes for the large variations in thresholds of the hafnia coating appear to be related to substrate preparation and will be investigated. Alternate methods for depositing hafnia (for instance, from a metal melt with O_2 ion assist) will be considered, as well as methods of recycling the spent scandia. Finally, all the work to date has been with 50-mm-diam test substrates. Tests will be performed on the lightweight transport-mirror material when that design has been finalized and the process technology transferred to the future 72" coating chamber, which will be installed to coat the OMEGA Upgrade optics.

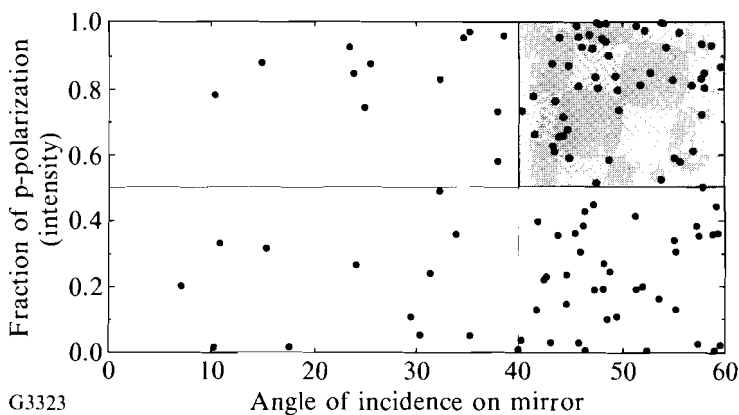


Fig. 51.25
The input polarization is plotted as a function of the incident angle for the transport mirrors in the two-mirror OMEGA Upgrade scheme. The shaded portion represents the mirrors with the highest damage probability and, therefore, those most likely to be coated with the more damage-resistant, scandia/silica, high-reflector coatings.

ACKNOWLEDGMENT

This work was supported by the U.S. Department of Energy Office of Inertial Confinement Fusion under agreement No. DE-FC03-85DP40200 and by the Laser Fusion Feasibility Project at the Laboratory for Laser Energetics, which is sponsored by the New York State Energy Research and Development Authority and the University of Rochester.

REFERENCES

1. LLE Review **44**, 219 (1990).
2. J. H. Apfel, *Appl. Opt.* **16**, 1880 (1977).

3. W. H. Lowdermilk and D. Milam, in *Excimer Lasers, Their Applications, and New Frontiers in Lasers* (SPIE, Bellingham, WA, 1984), Vol. 476, p. 143.
4. M. Kozlowski, R. Smith, and R. Wolfe, LLNL Internal Memo LDG 91-120, 19 November 1991.
5. G. E. P. Box, W. G. Hunter, and J. S. Hunter, *Statistics for Experimenters: An Introduction to Design, Data Analysis, and Model Building* (Wiley, New York, 1978).
6. W. H. Lowdermilk and D. Milam, *IEEE J. Quantum Electron.* **17**, 1888 (1981).
7. Dupont Co., Instruments/Biomedical Division, Newtown, CT 06470 – Model “Sorval GKM.”
8. J. D. Boyer, S. R. Foltyn, B. R. Mauro, and V. E. Sanders, in *Laser Induced Damage in Optical Materials: 1989*, Natl. Inst. Stand. Technol. (U.S.), Spec. Publ. 801 (U.S. Government Printing Office, Washington, DC, 1990), p. 417.
9. B. E. Newnam, S. R. Foltyn, D. M. Gill, and L. J. Jolin, in *Laser Induced Damage in Optical Materials: 1984*, Natl. Bur. Stand. (U.S.), Spec. Publ. 727 (U.S. Government Printing Office, Washington, DC, 1986), p. 342.
10. B. Liao, D. J. Smith, and B. McIntyre, in *Laser Induced Damage in Optical Materials: 1985*, Natl. Bur. Stand. (U.S.), Spec. Publ. 746 (U.S. Government Printing Office, Washington, DC, 1988), p. 305.

2.C An Externally Triggered, Single-Mode, Nd:YLF Laser Oscillator

Single-axial mode, high-brightness laser oscillators are of considerable interest for a variety of applications from nonlinear optics to laser-fusion lasers. The latter typically require such lasers for the generation of shaped pulses with the added requirement of accurate synchronization to other short-pulse lasers.

Mono-mode lasers^{1,2,3} have been reported widely in the literature over the past several years but reports on reliable mono-mode oscillators at 1053 nm (Nd:YLF) are less frequent. Recently, several reports on mono-mode lasers have taken advantage of efficient diode pumping and the recent discovery of low-loss, acousto-optically induced, unidirectional ring oscillators.¹ Unidirectional ring oscillators avoid spatial hole burning and are essential for crystalline media such as Nd:YLF, which cannot use such effective methods as are used in the unidirectional, non-planar Nd:YAG ring resonators,³ or linear resonators using circular polarization in the active medium.⁴ The diode-pumped Nd:YLF lasers reported have output energies that typically range in the μJ regime² with ≤ 1 -kHz repetition rates, but they have not been checked for external synchronizability, i.e., build-up time jitter of the Q -switched output pulse.

In this article we concentrate on reliable mono-mode oscillator performance with ~ 1 mJ output energy at very moderate repetition rates < 10 Hz. The oscillator has an externally triggered Q -switch permitting synchronization to a signal with tens-of-microseconds jitter relative to the flash-lamp trigger pulse. To this end we use a conventional, flash-lamp-pumped active medium (Nd:YLF) lasing at 1053 nm, which is ideally suited for amplification in large Nd:phosphate glass-amplifier chains. Mono-mode operation is assured using a combination of extended, low-intensity, pre-lase phase,⁵⁻⁷ unidirectional ring-laser configuration, and a single, 10-mm-thick, intra-cavity etalon. The pre-lase phase is controlled with an active feedback to suppress normal mode spiking prior to Q -switching. In addition, we have installed an active, interferometric, cavity-length control.⁸ This assures wavelength stability and increases the reproducibility of the laser-output characteristics such as amplitude, build-up time, and FWHM of the Q -switched pulse. Successful synchronization in this context implies a build-up time jitter of much less than the FWHM, i.e., typically $< 10\%$.

Experimental Setup

The stable, unidirectional ring cavity has an optical path length of ~ 86 cm (Fig. 51.26). The active medium is a 4-mm-diam, 60-mm-long, Nd:YLF rod with wedged end faces. The rod is oriented so it lases at 1053-nm wavelength. A low-pressure xenon lamp (1.5-in. arc length) is used in a diffuse, close-coupled pump cavity. Transverse modes are suppressed by a 1.5-mm aperture, and unidirectional operation is achieved with a Faraday isolator causing a $\sim 20^\circ$ rotation of the plane of polarization. A single KD*P Pockels cell ($V_{\lambda/2} = 8$ kV) is used for controlling intracavity losses during the pre-lase period and for Q -switching. A 10-mm-thick intracavity etalon (reflectivity $R = 50\%$ at 1053 nm) suppresses higher longitudinal modes. The temperature of the etalon is controlled to approximately $\pm 0.1^\circ\text{C}$.

All components are mounted on a completely enclosed invar table. Mechanical stability of the laser resonator is further enhanced by using heavy mounts and minimizing the number of positioning adjustments. One of the cavity mirrors is mounted on a piezoelectric translator (PZT) embedded in an Al block for stability and for suppression of low-frequency mechanical resonances.

To provide long-term stability through compensation for temperature drifts, we use an active control system incorporating a frequency-stabilized HeNe interferometer (Fig. 51.26). The 633-nm wavelength provides a resolution of almost twice that of the Nd:YLF wavelength of 1053 nm. Part of the HeNe beam is reflected at the output coupler and interferes with the remainder after one round-trip. The three high-reflectance mirrors are dichroic with $R = 100\%$ at 1053 nm and 80% at 633 nm, and the output coupler has $R = 90\%$ at 1053 nm and 25% at 633 nm. A half-wave plate and a collimator are used to optimize the HeNe fringe contrast, which also depends on the applied Pockels cell voltage. An enlarged image of the HeNe fringes is incident on two closely spaced photodiodes such that the diodes straddle a fringe. The photodiode signals are differentially amplified, processed, and fed back to the PZT (Burleigh model PZ-70 HV driver and PZT model PZ-80 with 7- μm maximum excursion). The open feedback circuit response has a dead time of $t_d \approx 200$ μs and a rise time of $t_r \approx 2$ ms. The

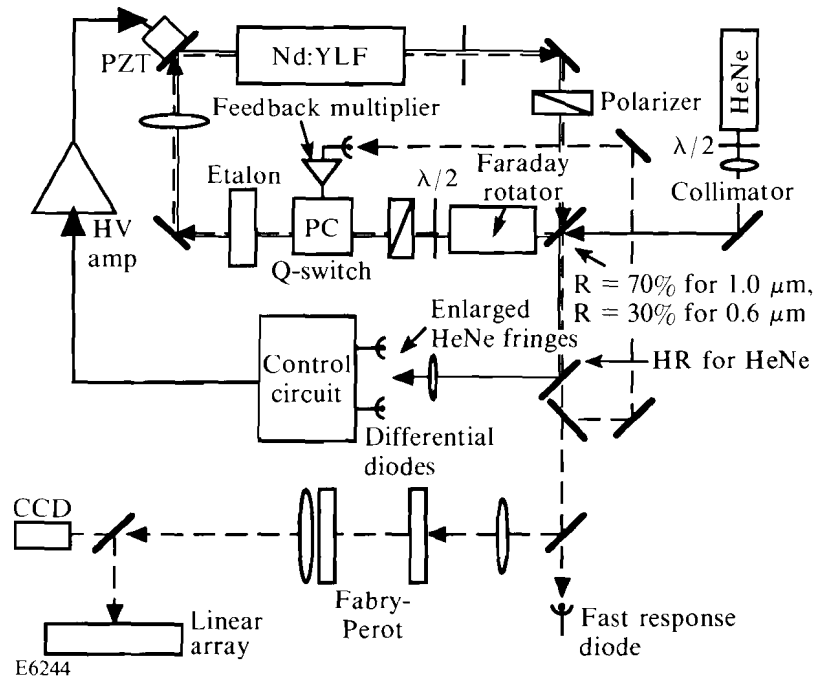


Fig. 51.26

Experimental setup for unidirectional, single-axial-mode, Nd:YLF laser with length feedback control and extended low-intensity pre-lase feedback control.

optimum operating parameters for this feedback circuit are determined using a method proposed by Oppelt.⁹ The circuit has a bandwidth of ~ 200 Hz, enough to respond to typical long-term temperature and PZT drifts of the optical path length. The length control is not completely dispersion-free and can give rise to some residual, uncompensated error signal. This is a result of the differential wavelength-dependent, thermo-optic response of the laser and KD*P crystals, which tend to compensate each other, although not completely.

With the control loop closed, the laser can be tuned to operate at the desired wavelength by translating the entire differential diode assembly across the HeNe fringe pattern. This simple feedback system is capable of maintaining the Nd:YLF cavity length to within $\leq 0.2 \lambda_{\text{HeNe}}$ over periods of several hours. The time limits on the stabilization are set by the maximum excursion of the PZT. The ambient temperature control in our experimental area was so poor as to set the ultimate limits on the time period (2 to 3 hours) before the feedback ran out of PZT travel.

Part of the $1\text{-}\mu\text{m}$ laser beam is used in another feedback loop to generate an extended pre-lase phase of $\leq 100 \mu\text{s}$. This feedback circuit is a high-voltage cascade, open-loop amplifier connected to a Pockels cell. The open-loop amplifier combined with a cascade of several decoupled MOSFET transistors allows both feedback for the pre-lase phase and for the subsequent Q-switch. The small-signal bandwidth of this system is 340 kHz (large-signal bandwidth ~ 130 kHz) with a typical response time of ~ 300 ns.

A flat-plate Fabry-Perot (FP) interferometer and a fast vacuum photodiode are used to analyze and characterize the temporal and spectral behavior of the Nd:YLF laser output.

The FP interferometer (Burleigh model RC-110) has an instrumental finesse of $F_I \approx 90$. The plate spacing of ~ 10 cm is chosen such that adjacent intracavity etalon modes of the Nd:YLF oscillator are centered between adjacent FP orders, while adjacent oscillator modes appear closely spaced to, but well-resolved from, adjacent FP orders. Thus, the fringe location clearly identifies its source. To avoid speckle a negative lens of short focal length ($f = -5$ cm) is used to illuminate the interferometer resulting in parabolic intensity distribution of the output. A 1-m lens then images the FP fringe pattern onto a linear photodiode array.

The linear photodiode array (EG&G PARC 1453 AC) has 1024 pixels with a 25- μm diode spacing and 2.5-mm diode height. The array is operated at -5°C and can achieve a dynamic range of $\sim 15,000$. The array is centered on the FP fringe pattern but its height distorts the fringes and adds asymmetric shoulders near the origin of the circular FP pattern.

The temporal behavior of the laser output is analyzed for high-frequency modulation and build-up time jitter. A vacuum photodiode (Hamamatsu R1328U-01) with a rise time of $t_r \approx 100$ ps is displayed on a 4.5-GHz Tektronix SCD 5000 transient digitizer. The cutoff frequency of the detection system is around 10 GHz, which is close to the free spectral range (FSR) of the 1-cm intracavity etalon and greatly exceeds the 350-MHz longitudinal-mode spacing of the ring resonator. The build-up time jitter of the Q -switched pulse with respect to the Q -switch trigger is monitored with a HP-4220 PIN diode and a Tektronix 2440 oscilloscope. The two scope traces and the linear-array FP data are acquired by a personal computer for subsequent statistical analysis.

Experimental Results

For diagnostic test purposes, the setup shown in Fig. 51.26 is used with the laser-output feedback loop disabled and the Q -switch optically triggered on top of the first relaxation oscillation. Varying the flash-lamp pump energy and the bias voltage on the Pockels cell, the FWHM of the Q -switched pulse can be varied between 20 and 100 ns.

Figure 51.27 shows Fabry-Perot fringes obtained with the linear array for a typical mono-mode shot and two different multi-mode shots. The center of the FP fringe pattern is to the right of the traces displayed. The top line represents a clean mono-mode shot. The shoulder to the right of each FP fringe is mostly instrumental although it may also contain a small frequency drift as a result of heating of the laser rod during the pre-lase period. This period is well below the response time of the HeNe interferometric-length control system. The dotted line is a FP trace in the presence of a weak adjacent oscillator mode, and the bottom curve shows the simultaneous presence of a neighboring oscillator mode and a neighboring mode of the intracavity etalon.

The corresponding oscilloscope traces just before the peak of the Q -switched pulse are shown in Fig. 51.28. For illustration purposes, the traces are shifted vertically. The mono-mode pulse (top line) exhibits no modulation while the middle trace shows the 340-MHz modulation typical for the presence of two neighboring oscillator modes. The bottom trace corresponds to the bottom trace in Fig. 51.27 and shows the 340-MHz modulation with a superposed weak, but clearly identifiable, 10.3-GHz modulation caused by the simultaneous presence of a second intracavity etalon mode. The amplitude of the 10.3-GHz modulation is drastically reduced by the finite bandwidth of the detection system.

For the long-term stability experiments we have chosen to analyze the FP traces only since the correspondence of the oscilloscope and FP traces has been so clearly demonstrated in Figs. 51.27 and 51.28. For these experiments the cavity-length stabilization feedback circuit is engaged. The Q -switch trigger is delayed by $\sim 40 \mu\text{s}$ relative to the initial rise in intracavity laser intensity. However, to simulate the external trigger capability, the Q -switch is actually triggered from the flash-lamp current pulse.

Fig. 51.27
Fabry-Perot traces taken with a linear diode array for single-mode and multi-mode emission from the oscillator. (Free spectral range of the Fabry-Perot interferometer is $\lambda_{\text{FSR}} \approx 1.5 \text{ GHz}$.) The single-mode response has an extended foot on one side, which appears to be caused by heating of the laser rod during the extended pre-lase period prior to Q -switching. Multi-mode behavior of this oscillator is obtained only if the intensity-feedback control is disabled.

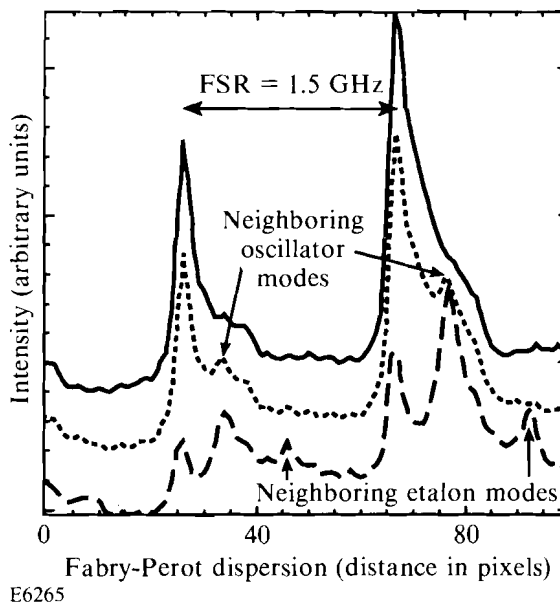


Figure 51.29 displays the results of a 6-h stability test where the laser was continuously operated at a 5-Hz repetition rate and data were recorded every 2 min. The figure shows a cross section of the first four FP fringes to one side of the zeroth-order fringe. The FSR of the FP is $\sim 1.5 \text{ GHz}$. A small amount of slow frequency drift is clearly seen in these records but no multi-mode shots have ever been observed under these conditions. This residual frequency drift is caused by dispersion inside the laser cavity between the $1\text{-}\mu\text{m}$ laser pulse and the 633-nm HeNe interferometer. However, any mode-jumping to neighboring cavity or etalon modes is very distinct as will be seen later.

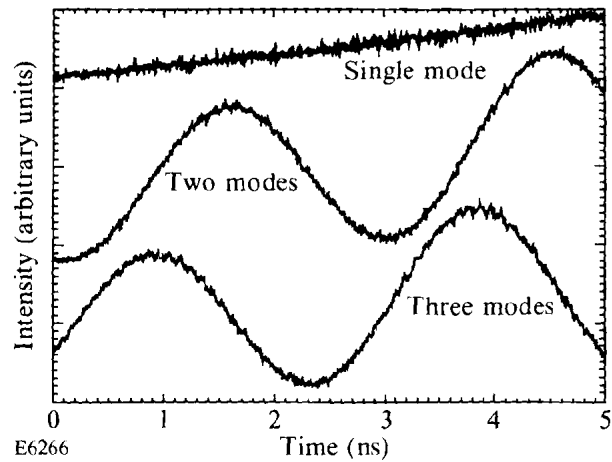


Fig. 51.28
Fast oscilloscope traces of the Q -switched laser output corresponding to the Fabry-Perot traces shown in Fig. 51.27.

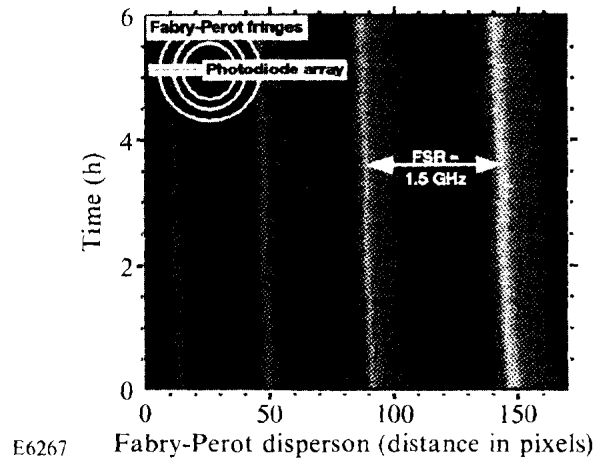


Fig. 51.29
Long-term stability test of mono-mode output: first four orders of the Fabry-Perot interferometer ($\lambda_{FSR} \approx 1.5$ GHz) taken with a linear diode array. The laser was operated at 5 Hz and data were recorded every 2 min. (For explanation of shoulders see Fig. 51.27.)

The build-up time jitter (time between Q -switch initiation and pulse peak) is shown in Fig. 51.30(a). The corresponding amplitudes and FWHM are shown in Fig. 51.30(b). For these experiments the laser is again Q -switched after a 40- μ s pre-lase phase at a data acquisition rate of one shot per minute (one out of every 300 actual shots) for a total of ~ 160 recorded shots. The cavity-length feedback loop is active. The corresponding FP traces in Fig. 51.30(c) indicate single-mode operation with a slight frequency drift. This frequency drift reflects a change in the effective cavity length as a result of temperature rise, which could not be completely compensated by the cavity-length feedback circuit because of dispersion between 633 nm (HeNe interferometer) and 1053 nm (Nd:YLF laser). The average build-up time for this typical run is 521.45 ± 8.40 (2%) ns, the peak intensity is 4.18 ± 0.24 (6%) (arbitrary units), and the FWHM is 99.9 ± 2.88 (3%) ns. The corresponding peak-to-valley (p-t-v) ranges are 39 ns, 1.12 arbitrary units (27%), and 16 ns (16%).

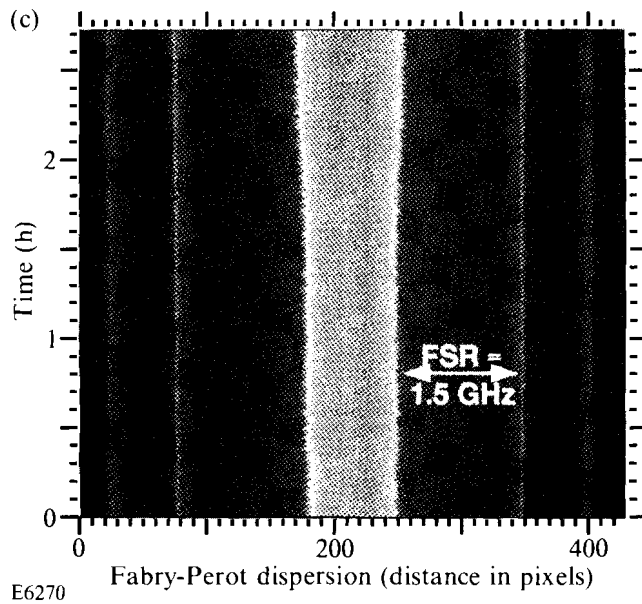
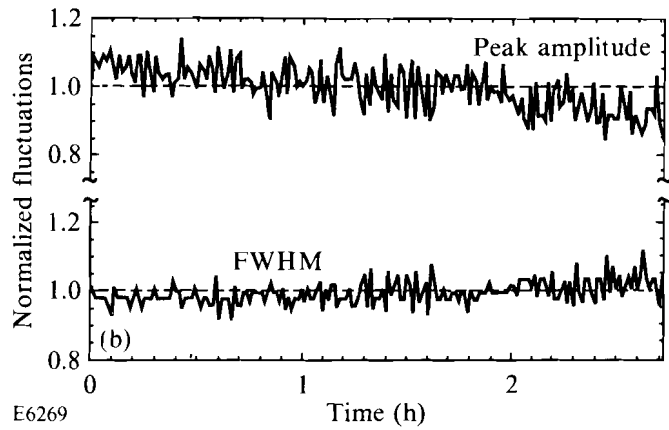
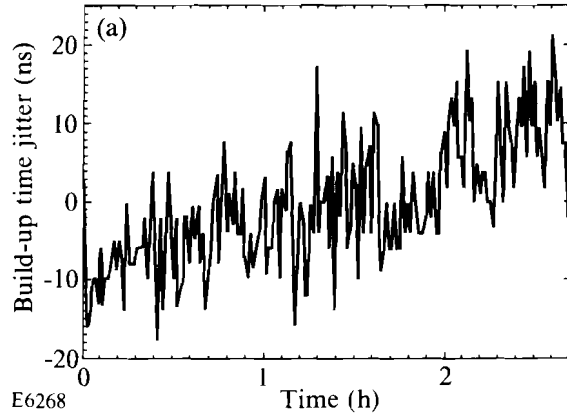


Fig. 51.30
 (a) Build-up time fluctuations around the average for *Q*-switched pulses with active laser-cavity-length feedback control and low-intensity feedback control during the pre-lase phase for suppression of normal-mode spiking. (b) Fluctuations of the peak intensity and FWHM of the *Q*-switched pulses and Fabry-Perot fringe cross sections (c) for the same series of shots ($\lambda_{\text{FSR}} \approx 1.5$ GHz).

Figure 51.31 demonstrates the clear correlation between mode-hopping and fluctuations in amplitude, FWHM, and build-up time. For this purpose the cavity-length feedback circuit is disabled but the pre-lase intensity feedback control remained active. Figure 51.31 displays the results for 95 shots taken at a data acquisition rate of 1 shot per min (one out of every 300 actual shots). The

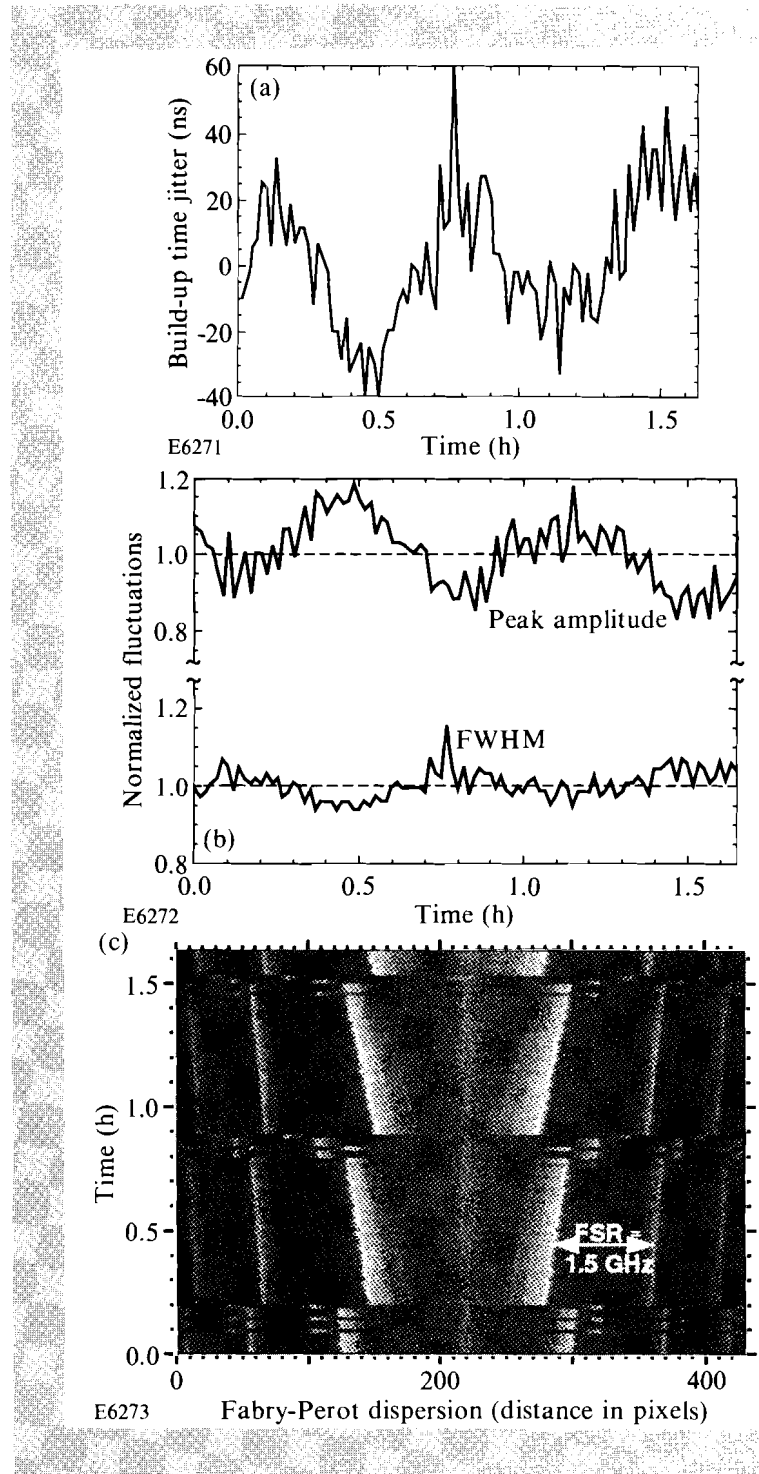


Fig. 51.31 Build-up time jitter (a), peak amplitude and FWHM fluctuations (b), and Fabry-Perot data (c) for mono-mode laser operation with intensity feedback control during the pre-lase phase, but without length stabilization. The gradual expansion of the optical path length (presumably caused by heating up of the active medium) is reflected in all three figures leading to mode-hopping and involving neighboring oscillator modes and neighboring intracavity etalon modes. Mode-hopping is accompanied by large build-up time jitter and significant amplitude fluctuations.

laser is again Q -switched $\sim 40 \mu\text{s}$ into the pre-lase phase. Under these conditions, the laser tends to mode-hop roughly every 40 min because of an apparent constant change in temperature over the whole of the recording time. Close inspection indicates that around the time of mode-hopping the laser jumps several times between adjacent laser cavity and intracavity etalon modes before settling down on another laser-cavity mode. Ignoring for the moment the correlation between mode-hopping and the Q -switch pulse parameters, the fractional rms and peak-to-valley fluctuations [build-up time: 6% (30% p-t-v), FWHM: 4% (20% p-t-v), and peak amplitude: 9% (34%)] are noticeably larger for the mono-mode laser without length-feedback control. However, in none of the shots is there any evidence for the simultaneous presence of two modes as was observed in Figs. 51.27 and 51.28 where the feedback control was disabled and the pre-lase phase was ended at the top of the first relaxation oscillation. Thus, mono-mode operation by itself does not require active-length control of the oscillator but it is required for more reproducible Q -switch amplitude and build-up time performance.

Varying the length of the pre-lase phase before Q -switching beyond the time at which the relaxation oscillations are almost fully damped ($\sim 40 \mu\text{s}$) degrades the build-up time jitter characteristics slightly ($\sim 5 \text{ ns}$ additional jitter) while hardly affecting the amplitudes and FWHM of the output pulses or their standard deviations.

Summary

We have developed a highly reliable, reproducible, externally triggerable, single-mode, flash-lamp-pumped Nd:YLF laser system with negative, intracavity intensity feedback. Mono-mode operation can be maintained over periods of many hours. Adding another feedback control on the cavity length increases the output stability of the laser-pulse characteristics and forces lasing at a constant and selectable wavelength, also over periods of hours.

ACKNOWLEDGMENT

This work was supported by the U.S. Department of Energy Office of Inertial Confinement Fusion under agreement No. DE-FC03-85DP40200 and by the Laser Fusion Feasibility Project at the Laboratory for Laser Energetics, which is sponsored by the New York State Energy Research and Development Authority and the University of Rochester.

REFERENCES

1. Yu. D. Golyaev, A. A. Zadernovskii, and A. L. Livintsev, *Sov. J. Quantum Electron.* **17**, 583 (1987); R. Roy, P. A. Schulz, and A. Walther, *Opt. Lett.* **12**, 672 (1987); W. A. Clarkson, A. B. Neilson, and D. C. Hanna, *Opt. Lett.* **17**, 601 (1992).
2. L. J. Bromley and D. C. Hanna, *Opt. Lett.* **16**, 378 (1991); W. A. Clarkson and D. C. Hanna, *Opt. Commun.* **81**, 375 (1991); W. A. Clarkson and D. C. Hanna, *Opt. Commun.* **84**, 51 (1991).
3. T. J. Kane and R. L. Byer, *Opt. Lett.* **10**, 65 (1985).
4. Y. K. Park, G. Giuliani, and R. L. Byer, *Opt. Lett.* **5**, 96 (1980); P. Esherick and A. Owyong, *J. Opt. Soc. Am. B* **4**, 41 (1987).

5. D. J. Kuizenga, *IEEE J. Quantum Electron.* **17**, 1694 (1981); D. J. Kuizenga and A. E. Siegman, *IEEE J. Quantum Electron.* **6**, 694 (1970); D. J. Kuizenga and A. E. Siegman, *IEEE J. Quantum Electron.* **6**, 709 (1970); G. B. Michelangeli *et al.*, *Opt. Commun.* **65**, 283 (1988).
6. R. P. Johnson, N. K. Moncur, and L. D. Siebert, in *Proceedings of the International Conference on Lasers '87*, edited by F. J. Duarte (STS Press, McLean, VA, 1988), p. 432; I. N. Ross *et al.*, *IEEE J. Quantum Electron.* **17**, 1653 (1981).
7. D. C. Hanna, B. Luther-Davies, and R. C. Smith, *Electron. Lett.* **8**, 369 (1972); I. Will, Ph.D. Dissertation, Technische Universität Berlin, Berlin, Germany, 1991.
8. An alternative approach to cavity-length control has been reported by S. B. Darack, D. R. Dykaar, and G. T. Harvey, *Opt. Lett.* **16**, 1677 (1991).
9. J. E. Gibson, *Nonlinear Automatic Control* (McGraw-Hill, New York, 1963); "Translations of Papers on Stability of Nonlinear Feedback Control Systems," Natl. Bur. Stand. (U.S.), Spec. Publ. 1691 (U.S. Government Printing Office, Washington, DC, 1952); J. G. Truxal, *Automatic Feedback Control System Synthesis* (McGraw-Hill, New York, 1955), p. 566.

Section 3

NATIONAL LASER USERS FACILITY NEWS

NLUF activity during the third quarter of FY92 included experiments conducted by the University of Florida and the University of Maryland on the OMEGA target chamber. These experiments will continue throughout the remainder of OMEGA's shot schedule.

C. Hooper from the University of Florida is working with LLE scientists to study x-ray spectroscopy from laser-imploded targets. The goal of this experiment is to use atomic spectroscopy from the core of imploded targets to measure the temperature and density of the core. Current targets in use are either filled with pure Ar or with an Ar/D₂ mixture. Two time-resolved x-ray spectrographs are used to measure the x-ray spectrum during the target implosion. The experimental data are taken to the University of Florida and analyzed with codes developed to understand line emission from hot dense matter.

H. Griem and **J. Moreno** from the University of Maryland are working with **P. Jaanimagi** from LLE to measure the time-dependent emission of x rays from Ne-filled targets. The group at the University of Maryland has developed a theory of *k*-shell emission from dense matter. This experiment uses targets with both Ne and D₂/Ne fills. A flat-field grating is used as the input to a streak camera to measure the Ne *k*-shell emission during the target implosion. The data are analyzed at both the University of Maryland and LLE.

GDL is now undergoing a refurbishment. This is to continue into the first quarter of FY93 and it should be ready for target experiments during FY93. The

current OMEGA target chamber will become the new GDL target chamber and will be available for single-beam 1054-nm and 351-nm experiments. The system will come up without a probe beam. This is to be added after the completion of the OMEGA Upgrade.

Remaining FY92 experiments by Syracuse University, the University of California at Davis, and the Naval Research Laboratory are being scheduled. They will get system time during the final OMEGA operating period.

ACKNOWLEDGMENT

This work was supported by the U.S. Department of Energy Office of Inertial Confinement Fusion under agreement No. DE-FC03-85DP40200.

Section 4

LASER SYSTEM REPORT

4.A GDL Facility Report

There were 227 GDL laser shots during the third quarter of FY92. The University of Illinois used 62 target shots for a NLUF experiment; 119 shots were used for laser-damage testing on laser optics; there were 37 laser-system test shots, and finally, 9 miscellaneous target shots were taken. The modifications on GDL to conduct the OMEGA Upgrade prototype tests began on 22 May.

The shot summary for the GDL laser this quarter is as follows:

Laser system	37
Target	<u>190</u>
TOTAL	227

4.B OMEGA Facility Report

The OMEGA system fired 470 shots during the third quarter of FY92, including shots for laser testing, diagnostics development, implosion experiments, and NLUF user experiments. We continued some of the power-conditioning refurbishment activity necessitated by the age of the system. In the first 14 years of its life, OMEGA has logged more than 24,000 shots.

Experiments conducted during this quarter included diagnostics-development shots for a high-speed, framing x-ray camera; a time-framed, x-ray ring aperture microscope; a neutron streak camera; MEDUSA system calibration; and x-ray backlighting. Implosion experiments were carried out with surrogate cryogenic CD shells and on deuterium-filled CH targets. NLUF experiments from the University of Maryland were also conducted.

The shot summary for the OMEGA laser this quarter is as follows:

Driver line	292
Laser development	82
Target	93
Software test	<u>3</u>
TOTAL	470

ACKNOWLEDGMENT

This work was supported by the U.S. Department of Energy Office of Inertial Confinement Fusion under agreement No. DE-FC03-85DP40200 and by the Laser Fusion Feasibility Project at the Laboratory for Laser Energetics, which is sponsored by the New York State Energy Research and Development Authority and the University of Rochester.

PUBLICATIONS AND CONFERENCE PRESENTATIONS

Publications

T. R. Boehly, R. S. Craxton, R. J. Hutchison, J. H. Kelly, T. J. Kessler, S. A. Kumpan, S. A. Letzring, R. L. McCrory, S. F. B. Morse, W. Seka, S. Skupsky, J. M. Soures, and C. P. Verdon, "The Upgrade to the OMEGA Laser System," in *Solid State Lasers III*, edited by G. J. Quarles (SPIE, Bellingham, WA, 1992), Vol. 1627, pp. 236–245.

D. K. Bradley, J. A. Delettrez, and C. P. Verdon, "Measurements of the Effect of Laser Beam Smoothing on Direct-Drive Inertial-Confinement-Fusion Capsule Implosions," *Phys. Rev. Lett.* **68**, 2774 (1992).

D. L. Brown, W. Seka, and S. Letzring, "Toward Phase Noise Reduction in a Nd:YLF Laser Using Electro-Optic Feedback Control," in *Solid State Lasers II* (SPIE, Bellingham, WA, 1991), Vol. 1410, pp. 209–214.

P. C. Cheng, H. G. Kim, and T. H. Lin, "The Study of Silica Deposition in the Leaf Blade of *Zea mays* L. by X-Ray Contact Microradiography and Confocal Microscopy," in *X-Ray Microscopy III*, edited by A. Michette, G. Morrison, and C. Buckley (Springer-Verlag, Berlin, 1992), Vol. 67, pp. 417–422.

T. Gong and P. M. Fauchet, "Femtosecond Nonlinearities and Hot-Carrier Dynamics in GaAs," in *Ultrafast Processes in Spectroscopy 1991*, edited by A. Laubereau and A. Seilmeier, Institute of Physics Conference Series No. 126 (IOP Publishing Ltd., Bristol, England, 1992), pp. 317–324.

- J. W. Herman and H. E. Elsayed-Ali, "Time-Resolved Study of Surface Disorder of Pb(110)," *Phys. Rev. Lett.* **68**, 2952 (1992).
- T. Juhasz, H. E. Elsayed-Ali, X. H. Hu, and W. E. Bron, "Time-Resolved Thermorefectivity of Thin Gold Films and Its Dependence on the Ambient Temperature," *Phys. Rev. B* **45**, 13819 (1992).
- J. H. Kelly, M. J. Shoup III, M. D. Sheldon, and S. T. Bui, "Design and Energy Characteristics of a Multisegment Glass Disk Amplifier," in *Solid State Lasers II*, edited by G. Dubé (SPIE, Bellingham, WA, 1991), Vol. 1410, pp. 40–46.
- J. H. Kelly, M. J. Shoup III, and M. M. Tedrow, "The Effect of Ionic and Particulate Platinum on the Performance of Large-Aperture Nd:Phosphate Glass Rod Amplifiers," in *Solid State Lasers III*, edited by G. J. Quarles (SPIE, Bellingham, WA, 1992), Vol. 1627, pp. 175–181.
- J. H. Kelly, M. J. Shoup III, M. M. Tedrow, and K. Thorp, "Energy Transport in a Modern Disk Amplifier," in *Solid State Lasers III*, edited by G. J. Quarles (SPIE, Bellingham, WA, 1992), Vol. 1627, pp. 286–297.
- H. Kim, B. Yaakobi, J. M. Soures, and P. C. Cheng, "Laser-Produced Plasma as a Source for X-Ray Microscopy," in *X-Ray Microscopy III*, edited by A. Michette, G. Morrison, and C. Buckley (Springer-Verlag, Berlin, 1992), pp. 47–53.
- Y. Lin, W. Seka, J. H. Eberly, H. Huang, and D. L. Brown, "Experimental Investigation of Bessel Beam Characteristics," *Appl. Opt.* **31**, 2708 (1992).
- M. K. Prasad, K. G. Estabrook, J. A. Harte, R. S. Craxton, R. A. Bosch, Gar. E. Busch, and J. S. Kollin, "Holographic Interferograms from Laser Fusion Code Simulations," *Phys. Fluids B* **4**, 1569 (1992).
- R. W. Short and E. M. Epperlein, "Thermal Stimulated Brillouin Scattering in Laser-Produced Plasmas," *Phys. Rev. Lett.* **68**, 3307 (1992).
- M. J. Shoup III, J. H. Kelly, M. M. Tedrow, F. A. Rister, and K. A. Thorp, "Mechanical Design of 15- and 20-cm Clear-Aperture Disk Amplifiers for the OMEGA Upgrade," in *Solid State Lasers III*, edited by G. J. Quarles (SPIE, Bellingham, WA, 1992), Vol. 1627, pp. 252–259.
- M. J. Shoup III, S. D. Jacobs, J. H. Kelly, C. T. Cotton, S. F. B. Morse, and S. A. Kumpan, "Specification of Large Aperture Nd:Phosphate Glass Laser Disks," in *Solid State Lasers III*, edited by G. J. Quarles (SPIE, Bellingham, WA, 1992), Vol. 1627, pp. 192–201.
- M. D. Skeldon, R. S. Craxton, T. J. Kessler, W. Seka, R. W. Short, S. Skupsky, and J. M. Soures, "Efficient Harmonic Generation with a Broadband Laser," in *IEEE J. Quantum Electron.* **28**, 1389 (1992).
- M. D. Skeldon, S. T. Bui, S. A. Letzring, and W. Siryk, "Implementation of Pulse Shaping on the OMEGA Laser System," in *Solid State Lasers III*, edited by G. J. Quarles (SPIE, Bellingham, WA, 1992), Vol. 1627, pp. 246–251.
- R. Sobolewski, "Prospects for High- T_c Superconducting Optoelectronics," in *Superconductivity and Its Applications*, AIP Conference Proceedings 251, edited by Y. H. Kao, A. E. Kaloyeros, and H. S. Kwok (American Institute of Physics, New York, 1992), pp. 659–670.

Forthcoming Publications

Y. Lin and T. J. Kessler, "Raman Scattering in Air: A Four-Dimensional System Analysis," to be published in the *Proceedings of SPIE's OE/LASE*, Los Angeles, CA, 20–25 January 1992.

G. G. Luther and C. J. McKinstrie, "The Transverse Modulational Instability of Counterpropagating Light Waves," to be published in the *Journal of the Optical Society of America B*.

R. S. Marjoribanks, M. C. Richardson, P. A. Jaanimagi, and R. Epstein, "Electron Temperature Measurement in Laser-Produced Plasmas by Ratio of Isoelectronic Line Intensities," to be published in *Physical Review A*.

F. J. Marshall, J. G. Jernigan, T. Collins, J. F. Arens, and G. Pien, "Measuring Laser-Plasma X-Ray Emission Using Photodiode Arrays," to be published in the *Review of Scientific Instruments*.

P. S. Maruthi Sai, M. J. Levene, T. Gillbro, R. S. Knox, R. H. Hwang-Schweitzer, and S. Mahajan, "Time-Resolved Fluorescence of Phycoerythrocyanin-Containing Phycobilisomes from the Cyanobacterium *Westiellopsis Prolifica*," to be published in *Biophysical Journal*.

R. L. McCrory, J. M. Soures, J. P. Knauer, S. A. Letzring, F. J. Marshall, S. Skupsky, W. Seka, C. P. Verdon, D. K. Bradley, R. S. Craxton, J. A. Delettrez, R. Epstein, P. A. Jaanimagi, R. L. Keck, T. J. Kessler, H. Kim, R. L. Kremens, P. W. McKenty, R. W. Short, and B. Yaakobi, "Short-Wavelength-Laser Requirements for Direct-Drive Ignition and Gain," to be published in *Lasers and Particle Beams*.

R. L. McCrory, R. E. Bahr, D. K. Bradley, D. L. Brown, R. S. Craxton, J. Delettrez, R. Epstein, P. A. Jaanimagi, T. Kessler, J. P. Knauer, S. Letzring, F. Marshall, P. W. McKenty, W. Seka, S. Skupsky, J. M. Soures, C. P. Verdon, and B. Yaakobi, "Direct-Drive Implosion Experiments for Laser Fusion on OMEGA and the OMEGA Upgrade," to be published in *Lasers and Particle Beams*.

R. L. McCrory, "Laser-Driven ICF Experiments," to be published in *Nuclear Fusion by Inertial Confinement*.

R. L. McCrory, "Direct-Drive Implosion Experiments for Laser Fusion on OMEGA and the OMEGA Upgrade," to be published in the *Proceedings of the 21st ECLIM*, Warsaw, Poland, 21–25 October 1991.

R. L. McCrory, "Irradiation Uniformity Requirements for Direct-Drive Laser Fusion," to be published in the *SPIE Proceedings of the XIV International Conference on Coherent and Nonlinear Optics*, St. Petersburg, Russia, 24–27 September 1991.

C. J. McKinstrie and R. Bingham, "Stimulated Raman Forward Scattering and the Relativistic Modulational Instability of Light Waves in Rarefied Plasma," to be published in *Physics of Fluids B*.

C. J. McKinstrie and M. V. Goldman, "Three-Dimensional Instabilities of Counterpropagating Light Waves in Homogeneous Plasmas," to be published in the *Journal of the Optical Society of America B*.

- C. I. Moore, "Confinement of Electrons to the Center of a Laser Focus via the Ponderomotive Potential," to be published in the *Journal of Modern Optics*.
- J. Peatross, M. V. Fedorov, and D. D. Meyerhofer, "Laser Temporal and Spatial Effects on Ionization Suppression," to be published in the *Journal of the Optical Society of America B*.
- J. K. Samarabandu, R. Acharya, C. D. Edirisinghe, P. C. Cheng, H. Kim, T. H. Lin, R. G. Summers, and C. E. Musial, "Analysis of Multi-Dimensional Confocal Images," to be published in the *Proceedings of the SPIE Symposium "Biomedical Imaging,"* San Diego, CA, 24 February 1991.
- W. Seka, R. E. Bahr, R. W. Short, A. Simon, R. S. Craxton, D. L. Montgomery, and A. E. Rubenchik, "Nonlinear Laser-Matter Interaction Processes in Long-Scale-Length Plasmas," to be published in *Physics of Fluids B*.
- L. J. Shaw-Klein, S. D. Jacobs, S. J. Burns, and J. C. Lambropoulos, "Microstructural Control of Thin-Film Thermal Conductivity," to be published in the *Proceedings of the 23rd Boulder Damage Symposium on Optical Materials for High Power Lasers,* Boulder, CO, 23–25 October 1991.
- M. D. Skeldon and S. T. Bui, "The Temporal Mode Structure of a Regenerative Amplifier with Intracavity Etalons," to be published in the *Journal of the Optical Society of America B*.
- J. M. Soures, R. L. McCrory, T. R. Boehly, R. S. Craxton, S. D. Jacobs, J. H. Kelly, T. J. Kessler, J. P. Knauer, R. L. Kremens, S. A. Kumpan, S. A. Letzring, W. D. Seka, R. W. Short, M. D. Skeldon, S. Skupsky, and C. P. Verdon, "The OMEGA Upgrade Laser for Direct-Drive Target Experiments," to be published in *Lasers and Particle Beams*.
- J. M. Soures, "Solid State Lasers," to be published in *Nuclear Fusion by Inertial Confinement,* edited by G. Velerade, Y. Ronen, and J. M. Martinez-Val.
- J. M. Soures, "High-Technology Advances from LLE Research," to be published in the *Rochester Business Profiles Journal*.
- J. M. Soures, "The OMEGA Upgrade Laser Facility for Direct-Drive Experiments," to be published in the *Proceedings of the Fusion Power Associates Annual Meeting and Symposium,* Princeton, NJ, 25–26 June 1991, and in the *Journal of Fusion Energy*.
- J. Sweetser, T. J. Dunn, I. A. Walmsley, C. Radzewicz, S. Palese, and R. J. D. Miller, "Characterization of an FM Mode-Locked Nd:YLF Laser Synchronized with a Passively Mode-Locked Dye Laser," to be published in the *Journal of the Optical Society of America B*.
- C. J. Twomey, S.-H. Chen, T. Blanton, A. W. Schmid, and K. L. Marshall, "Solid Polymers Doped With Rare Earth Metal Salts. II. Thermal Behavior and Morphology of the Neodymium Acetate-Poly(ethylene Oxide) System," to be published in *Journal of Polymer Science, Polymer Physics Edition*.
- R. Vanderhaghen, P. M. Fauchet, A. Mourchid, and D. Hulin, "The Cooling Rate of Hot Carriers in Disordered Semiconductors," to be published in the *Proceedings of QELS '92,* Anaheim, CA, 10–15 May 1992.

Conference Presentations

H. Kim and P.-C. Cheng, "Confocal Microscopic Characterization of Laser-Fusion Target," Scanning 92, Atlantic City, NJ, 1–3 April 1992 (invited paper).

The following presentations were made at CLEO '92, Anaheim, CA, 10–15 May 1992:

S. Alexandrou, R. Sobolewski, and T. Y. Hsiang, "Picosecond Separation of Electrical Transients Propagated on a Bent Coplanar Waveguide."

J. Armstrong and T. J. Kessler, "Holographic Recording of Large Aperture High-Efficiency, High-Damage Threshold Transmission Diffraction Gratings."

T. R. Boehly, R. S. Craxton, R. J. Hutchison, J. H. Kelly, T. J. Kessler, S. A. Kumpan, S. A. Letzring, R. L. McCrory, S. F. B. Morse, W. Seka, S. Skupsky, J. M. Soures, and C. P. Verdon, "The Upgrade to the OMEGA Laser System."

T. Y. Hsiang, S. Alexandrou, C.-C. Wang, R. Sobolewski, S. Y. Chou, and Y. Liu, "Picosecond Characterization of Nanometer-Scale Metal-Semiconductor-Metal Photodiodes."

L. E. Kingsley and W. R. Donaldson, "Electro-Optic Imaging of Ultrafast, High-Voltage GaAs Photoconductive Switches in Lock-On Mode."

R. L. McCrory, "Direct-Drive Target Physics: An Overview" (invited presentation).

S. M. Mehta, B. C. Tóusley, P. J. Rodney, A. I. Lobad, and P. M. Fauchet, "Spectral Dynamics Leading to Additive Pulse Mode-Locking in the NaCl Color Center Laser."

The following presentations were made at QELS '92, Anaheim, CA, 10–15 May 1992:

T. Gong, K. B. Ucer, Y. Kostoulas, G. W. Wicks, and P. M. Fauchet, "Carrier-Carrier Interactions in the Presence of Dense Plasma in GaAs."

T. Gong, P. M. Fauchet, P. J. Kelly, and J. F. Young, "Subpicosecond Hot-Hole Dynamics in Highly-Excited GaAs."

R. Vanderhaghen, P. M. Fauchet, A. Mourchid, and D. Hulin, "The Cooling Rate of Hot Carriers in Disordered Semiconductors."

The following presentations were made at the Optical Interference Coatings, Fifth Topical Meeting, Tucson, AZ, 1–5 June 1992:

R. G. Carnes and D. J. Smith, "A Physical Vapor Deposition System for OMEGA Upgrade Optics."

R. J. Sczupak and D. J. Smith, "Techniques and Applications for Large Aperture Structured Thin Films."

D. J. Smith, A. W. Schmid, Z. R. Chrzan, and S. Papernov, "Optical Coatings for the OMEGA Upgrade Laser."

J. D. Traylor and W. T. Pawlewicz, "Optical and Durability Properties of Bi_2O_3 , Cr_2O_3 , HfO_2 , Ta_2O_5 , Y_2O_3 , and ZrO_2 ."

The following presentations were made at the Eighth International Conference on Ultrafast Phenomena, Antibes-Juan-Les-Pins, France, 8–12 June 1992:

T. Gong, K. B. Ucer, L. X. Zheng, G. W. Wicks, J. F. Young, P. J. Kelly, and P. M. Fauchet, "Femtosecond Carrier-Carrier Interactions in GaAs."

B. C. Tousley, S. M. Mehta, A. I. Lobad, P. J. Rodney, G. W. Wicks, and P. M. Fauchet, "Femtosecond Band Edge Carrier Dynamics in $\text{In}_{0.53}\text{Ga}_{0.47}\text{As}$."

S. D. Jacobs, "Progress at the Center for Optics Manufacturing," SPIE International Symposium on Optical Fabrication, Testing, and Surface Evaluation, Technical Conference 1720/75, Toyko, Japan, 10 June 1992.

D. D. Meyerhofer, S. Augst, B. Buerke, and J. Peatross, "Laser Ionization of Noble Gases: Polarization and Pulse-Width Effects," IQEC '92, Austria Center, Vienna, 14–19 June 1992.

C. Bamber, W. R. Donaldson, E. Lincke, and A. C. Melissinos, "A Pulse-Power Accelerator Using Laser-Driven Photoconductive Switches," Third Workshop on Advanced Accelerator Concepts, Long Island, NY, 14–20 June 1992.

J. C. Lambropoulos, "Thermal Conductivity of Thin Films and Polycrystals," 6th International Conference on Intergranular and Interphase Boundaries in Materials, Thessaloniki, Greece, 21–26 June 1992.

P. V. Schwartz, C. W. Liu, J. C. Sturm, T. Gong, and P. M. Fauchet, "Current Transport Properties of Semi-Insulating Oxygen-Doped Silicon Films for Use in High-Speed Photoconductive Switches," 1992 Electronic Materials Conference, Cambridge, MA, 24–26 June 1992.

ACKNOWLEDGMENT

The work described in this volume includes current research at the Laboratory for Laser Energetics, which is supported by New York State Energy Research and Development Authority, the University of Rochester, the U.S. Department of Energy Office of Inertial Confinement Fusion under agreement No. DE-FC03-85DP40200, and other agencies.

UNIVERSITY OF
ROCHESTER